A V-ATPase complex, required for biogenesis of a lysosome-related organelle (LRO) in *Tetrahymena thermophila*, disassembles during LRO maturation

Ajay Pradhan[1,2] Niraj Tadasare[1] Debolina Sarkar[1,2] Lavan K. Bansal[1] Aaron P. Turkewitz [3] Santosh Kumar [1,2,4 *]

[1]National Centre for Cell Science, NCCS Complex, Savitribai Phule Pune University Campus, Ganeshkhind Road, Pune 411007 Maharashtra, India

[2]Regional Centre for Biotechnology, NCR Biotech Science Cluster, Faridabad 121001 Haryana, India

[3]Department of Molecular Genetics and Cell Biology, The University of Chicago, Chicago IL USA 60637

[4]Lead contact
*Correspondence: sbalot@nccs.res.in, sbalot@gmail.com (S.K.)

Abstract
In the ciliate *Tetrahymena thermophila*, a subset of proteins are exocytosed via lysosome-related organelles (LROs) called mucocysts. Formation of many LROs depends on modulation of pH by vacuolar-type ATPases (V-ATPases). Here, we used expression profiling to identify a V-ATPase a-subunit that is targeted to mucocysts. Cells lacking the *V-ATPase-a1* gene are defective in mucocyst biogenesis and exocytosis. However, the requirement for this subunit may not be limited to the canonical role of V-ATPases in proton pumping, since we find no evidence that mature mucocysts are acidified. Consistent with this, we find that while the a1-subunit is present in both immature and mature mucocysts, several other V-ATPase subunits are absent from the latter. These data suggest that the V-ATPase complex disassembles during mucocyst maturation, and that the a1-subunit performs roles independent of the holo-complex. Cells lacking the a1-subunit are defective in the targeting of both structural and enzymatic mucocyst proteins, and moreover appear deficient in fusion between vesicles from the secretory and endocytic pathways that is a feature of normal mucocyst maturation.

Introduction:
All cell types secrete proteins and other molecules, and many cell types have evolved specialized pathways to tailor this secretion to physiological requirements. In eukaryotes, the predominant mechanism of secretion is the fusion of cytoplasmic vesicles with the plasma membrane, which causes the vesicle contents to be released exocytically into the cell exterior (1, 2). In animals, subsets of specific secretory proteins can be stored in different vesicular compartments and released via tightly regulated exocytosis. These storage compartments are derived from two prominent pathways. The first pathway generates dense core granules (DCGs), which are best known for regulating insulin secretion (3). DCG biogenesis includes the coalescence of cargo proproteins in the TGN from which they bud as immature granules, followed by a series of maturation steps to form the mature secretory granules. During maturation newly formed DCGs are acidified, activating processing enzymes that cleave precursor polypeptides to generate mature bioactive peptides (4–6). The bioactive peptides are

vital regulators of both metabolic and cognitive functions, among a wide variety of physiological roles in humans.

The second pathway produces a distinct class of secretory structures called lysosome-related organelles (LROs). Classical LROs comprise diverse membrane organelles, many associated with human diseases, that share features of late endosomes and lysosomes, but are functionally, morphologically, and/or compositionally distinct (7–9). The protein cargoes packaged in LROs rely on receptors and cytoplasmic adaptors for their selection (10–12). In mammals, LROs, such as Weibel-Palade bodies, melanosomes, acrosomes and platelet-dense granules, are vital structures and serve many functions, including regulated exocytosis (8, 13–17). Fully functional LROs are generated by a multistep process in which an immature organelle matures by acquiring additional cargo from both secretory pathways as well as traffic from endosomes (10, 12, 18). This process involves membrane and cytoplasmic proteins, including the AP-3 adaptor, the homotypic fusion and protein sorting (HOPS) complex, the small GTPases Rab32 and Rab38, the sorting receptor sortilin/VPS10, and three biogenesis of LROs (BLOC) complexes (11, 19–23). This kind of multi-step maturation is also characteristic of DCGs, such as those responsible for insulin storage in the endocrine pancreas(3). However, such granules have classically been thought to form directly from the trans golgi network (TGN), while LROs acquire much of their content from the endo-lysosomal system (8, 12, 24). It is worth noting that several recent studies have suggested mechanistic links between LRO and DCG formation, making the study of LROs even more important for advancing human health (25–31).

The ciliate *Tetrahymena thermophila*, like mammalian cells, has a complex network of endocytic and secretory compartments**.** One particularly prominent compartment in this ciliate is called mucocysts, which dock at the cell cortex and function as regulated secretory organelles, releasing their contents when cells are stimulated (11, 21, 31, 32). Based on evidence that mucocyst formation relies on mechanisms that function in lysosome formation (21, 31), mucocysts can be considered to belong to the very broad family of LROs, comparable to secretory LROs like Weibel-Palade bodies, melanosomes, and platelet-dense granules in mammalian cells, *Caenorhabditis elegans* gut granules and *Drosophila* eye pigment granules (30, 33–35).

The mucocyst cargo proteins are encoded by two multigene families: GRL (granule lattice) and GRT/IGR (granule tip/induced on granule regeneration; (36–38). GRL proteins are primarily filled in the lumen of mucocysts, which are transported to immature mucocysts as proproteins and then undergo proteolytic processing by key processing enzymes Cth3p and Cth4p to generate mature GRL proteins (32, 39). The processing of GRL proteins is essential for secretion because only mature GRL proteins can form a crystalline core that expands during exocytosis to extrude the mucocyst contents (37). While, GRT protein is concentrated at one end, at the tip that fuses the plasma membrane during exocytosis (38). The delivery of Cth3p and Grt/Igr proteins to mucocysts, but not Grl proteins, requires the sortilin/VPS10 receptor Sor4p and an endosomal SNARE known as Stx7l1p (Syntaxin 7-like) (11, 21, 31). The current model of mucocyst biogenesis in *T. thermophila* revealed that both Grl and Grt1mucocyst cargo proteins locate nonoverlapping vesicles in *Stx7l1* and *VPS8a* knockout cells (21, 31). Stx7l1p is a Qa-SNARE whose homologues are associated with vacuoles/LROs in different lineages (21), while VPS8ap is a subunit of the CORVET complex (31). Both VPS8ap and Stx7l1p are required for homotypic and/or heterotypic fusion of pro-Grls and non-Grlp proteins containing vesicles to generate immature mucocysts, which then go through maturation steps to produce mature mucocysts (21, 31). This maturation is dependent on processing enzymes and the AP-3 protein (21). However, this model is incomplete since many components of the mucocyst/LRO biogenesis pathway are unknown.

Vacuolar-type proton ATPase (V-ATPase) is a proton pump that transports H^+ (protons) across the membrane using the energy from ATP hydrolysis to acidify cellular compartments in eukaryotic cells (40, 41). V-ATPase activity is required for exocytosis in various species (42–44). Moreover, several lines of evidence have indicated that the processing and secretion of LRO contents are regulated via acidification by V-ATPases (43, 45, 46). For example, previous studies have suggested that V-ATPase function might be important for the appropriate processing and maturation of insulin (4, 47–49).

V-ATPases are composed of two domains, V_1 and V_0. V_1, the catalytic domain, is a 650-kDa peripheral macromolecular complex that is involved in ATP hydrolysis that generates the energy required for pumping protons and consists of $A_3B_3CDE_3FG_3H$ subunits. V_0 is a 260-kDa integral membrane protein complex that forms a proton channel and consists of $ac_8c'c''def$ and VOA1p in yeast (40, 41, 50). The V_1 and V_0 domain subunits together form a fully functional holo-V-ATPase complex. Holo-V-ATPase's enzyme activity is regulated by a unique process called reversible disassembly, in which the V_1 domain separates from the membrane-integral Vo domain (51, 52). In yeast and mammalian cells, reversible V-ATPase assembly and disassembly have been reported in response to different conditions, including glucose and amino acid starvation and refeeding (53–58). Additionally, the oxidative stress protein Oxr1 promotes disassembly of the holoenzyme and inhibits V-ATPase activity (59). Increasing assembly has been proposed as a cause of increased acidity throughout the endocytic route in mammalian cells (60). Reassembly of V-ATPase complex is facilitated by numerous components, such as the heterotrimeric chaperone complex "RAVE (Regulator of ATPases of Vacuolar and Endosomal membranes)" as well as glycolytic enzymes phosphofructokinase-I and aldolase (53, 58, 61–63).

V-ATPases are not unique to LROs but function to acidify a variety of endocytic and secretory pathways (41). For example, subunit-a isoforms play conserved functions in many stages of phagocytosis and endocytosis across various species (64, 65). While all V-ATPases act as proton translocases, they enable distinct functions in different compartments and are therefore likely to possess compartment-specific features. Most V-ATPase subunits in animal cells exist in multiple isoforms that are expressed in a tissue-specific manner (41), and isoform-specific activities or localization have been demonstrated in many organisms (40, 41, 66, 67). For example, two ‘B’ V-ATPase subunit isoforms (B1 and B2) are present in the human genome. B1 isoform is mostly found in the kidney and epididymis, whereas B2 isoform was localized in the brain. These isoforms are required for ATP hydrolysis during proton pumping (40). In mammals, the subunit-a has four isoforms: a1, a2, a3, and a4, encoded by Atp6v0a1, Atp6v0a2, Atp6v0a3 and Atp6v0a4 genes, respectively (68). These isoforms carry information that directs the V-ATPase to distinct cellular destinations (41, 65, 68–71). The isoforms (a1–a3) are expressed ubiquitously, while the a4 isoform is specifically expressed in some specific tissues. The isoforms a1, a2, and a3 are associated with coated vesicles, the Golgi apparatus/early endosomes, and late endosomes/lysosomes, respectively (40, 41, 66). The V-ATPase subunit a3 has also been localized to insulin-containing secretory vesicles in pancreatic islet cells, where it likely contributes to the acidic environment required for proteolytic processing of insulin (72). These results are highly indicative that V-ATPases are directly or indirectly involved in the secretion and proteolytic processing of insulin. In addition, the V-ATPase-a3 isoform is also involved in trafficking of LRO proteins via Rab-7 in osteoclasts (46, 69, 73). Therefore,-V-ATPases can be considered a key component of LROs. In yeast, distinct subunit-a isoforms in V-ATPases differ in proton pump energy-coupling efficiency, subcellular localization, and in the regulation of subunit association under cellular metabolic conditions

(74, 75). For example, only subunit-a has multiple isoforms in yeast, encoded by the *VPH1* and *STV1* genes (75, 76).

In this study, we used expression profiling to identify a vacuolar ATPase a-subunit in *T. thermophila* that is targeted to mucocysts. The targeting of mucocyst core proteins as well as a key processing enzyme, Cth3p, required for their proteolytic maturation are disrupted in *Δv-atpase-a1 cells, thus,* showing defects in both mucocyst biogenesis and exocytosis. Remarkably, the requirement for this subunit may not be due to the canonical role of V-ATPases in proton translocation to acidify intracellular compartments. Since we find no evidence that mucocysts are acidified. Moreover, several other subunits expected for an active holo-V-ATPase complex, are present in immature mucocysts, whereas mature mucocysts only have a subset of those subunits. These findings indicate that the V-ATPase complex disassembles during mucocyst maturation, and that the a1-subunit plays roles independent of the holo-complex. Further, our results suggest that V-ATPase-a1p functions during mucocyst formation to promote homotypic and/or heterotypic fusion of Grl1p and Grt1-containing vesicles. Our findings show that at least one V-ATPase subunit plays unique roles in LRO biogenesis.

Results

Expression profiling reveals co-regulation of mucocyst-associated proteins and V-ATPase-a1 subunit of the Vo domain of V-ATPase complex in *T. thermophila*

The *T. thermophila* macronuclear genome has more than 24,000 predicted genes, including 11 that encode the subunits of the V_1 domain and 12 that encode the subunits of the Vo domain of the V-ATPase complex (77, 78). To ask whether there might be mucocyst-specific subunits, we followed up on earlier findings that many genes encoding mucocyst proteins are highly coregulated under a variety of conditions (11, 32, 39, 79–81). We used the online tools at the Tetrahymena Functional Genomics Database (http://tfgd.ihb.ac.cn/) to identify V-ATPase subunits that are coregulated with known mucocyst-associated genes. We discovered that only a single gene, encoding the V-ATPase-a1p subunit (TTHERM_01332070) of V_o, was coregulated with known mucocyst-associated genes **(Figure 1A)** and therefore represented a strong candidate for a mucocyst-specific V-ATPase subunit. The *Tetrahymena* V-ATPase-a1p shares ~30% sequence identity with human subunit-a isoforms (a1p: ATP6V0A1, a2p: ATP6V0A2, a3p: ATP6V0A3 and a4p: ATP6V0A4). The relationships between the *Tetrahymena* V-ATPase-a1 and its homologs in other organisms are shown in a phylogenetic tree **(Figure 2A)**. Consistent with the phylogenetic analysis, the predicted structure of the *T. thermophila* V-ATPase-a1p was strikingly similar to those of homologous V-ATPase-a subunits (shown for Opisthokonts) with 100% confidence and 85% coverage **(Figure 2B).** Structures similar to the *T. thermophila* V-ATPase-a1p in the AlphaFold Protein Structure Database (green) included the V-ATPase-a from Saccharomyces cerevisiae (yellow; A0A7I9G792) and Mus musculus (red; Q9Z1G4), the former with an 84% per-residue model confidence score (pLDDT) **(Figure 2C-D)**.

In addition to TTHERM_01332070, the *T. thermophila* genome contains five additional paralogs, which we named *a2* (TTHERM_00463420), *a3* (TTHERM_00266570), *a4* (TTHERM_00372530), *a5* (TTHERM_01005210) and *a6* (TTHERM_01014710). These paralogs are significantly diverged, with a maximum of 45% amino acid sequence identity to the a1 paralog **(Figure S1)**. Six of the seven predicted transmembrane (TM1 to TM7) helical domains of the a1 protein **(Figure 1B)** show structural homology with the corresponding domains of the other paralogs. The exception is the TM5 domain, which appears to be

structurally divergent **(Figure 1C)**. None of these paralogs is coregulated with genes that encode mucocyst cargo proteins **(Figure 1D)**, consistent with the idea that they belong to complexes specialized for and functioning in other cellular compartments.

V-ATPase-a1p localizes to mucocysts

To ask whether the *Tetrahymena* a1 subunit, implied via coregulation to be associated with mucocysts, is physically associated with this compartment, we endogenously tagged the *T. thermophila* copy of V-ATPase-a1p with 2 x mNeon [V-ATPase-a1p(N)]. The localization of the fluorescent protein was examined by confocal microscopy and compared with mucocyst markers. In live cells, V-ATPase-a1p(N) localized to linear arrays of fluorescent puncta at the cell surface, consistent with its accumulation in mucocysts **(Figure 3A, left panel, inset and Movie S1)**. In cross sections of the same cells, docked mucocysts are seen as elongated vesicles **(Figure 3A, right panel, inset and Movie S1)**. We found an identical pattern when the protein was endogenously tagged with GFP [V-ATPase-a1p(G)] rather than mNeon **(Figure S2)**. The expression in *Tetrahymena* of a fusion protein of the expected size was confirmed by immunoprecipitation followed by Western blotting **(Figure 3B)**.

Localization of V-ATPase-a1p(N) to mucocysts was further confirmed by co-localizing the V-ATPase-a1p(N) in cells co-expressing fluorescently-tagged copies of two different mucocyst cargo proteins, Igr1p-mCherry and Grl3p-mCherry, which showed a clear localization of V-ATPase-a1p(N) in the docked mature mucocysts at the cell cortex **(Figure 3C-D, inset)**. In optical cross sections of the same cells, some overlap between the V-ATPase-a1 and mucocyst cargo signals was observed (**Figure 3C-D, Ci and Di)**. The partial overlap is due to the fact that a significant proportion of V-ATPase-a1p(N) localizes to heterogeneous cytoplasmic puncta at some distance from the cortex (which we call "non-cortical"), some of which contain Igr1p-mCherry or Grl3p-mCherry **(Figure 3C-D)**. Approximately 75% of V-ATPase-a1p(N) is present in the non-cortical compartments, with the remaining quarter located at the cell cortex in the docked mucocysts (**Figure 3E-F**). To ask whether the same were true for all V-ATPase-a1 paralogs in *T. thermophila*, notwithstanding their very different transcriptional profiles, we similarly analyzed the localization of V-ATPase-a2p. This protein was found to be localized mostly at the plasma membrane and not in a mucocyst-like array **(Figure S3)** nor co-localized with the mucocyst marker Grl3p **(Figure S3)**.

V-ATPase-a1p is partially associated with endosomes but not with lysosomes

The targeting of selective membrane-associated and soluble lumenal cargo to classical LROs, and probably to mucocysts as well, involves multiple pathways. These include vesicle budding from the TGN, to deliver cargo to immature LROs. For mucocysts, the GRL proteins are likely to arrive via this route (31). A second route involved in mucocyst cargo delivery involves endosomes, and Grt1p, Igr1p, and Cth3p appear largely to follow this pathway (21, 31). V-ATPase-a1p could potentially be delivered by either of these pathways. To gain insight into this question, we sought to characterize the non-cortical V-ATPase-a1p(N)-positive structures, since these could represent transport intermediates.

Cells expressing V-ATPase-a1p(N) were incubated with FM4-64, previously shown to label endosomes in *Tetrahymena* (32). After an initial pulse with FM4-64, cells were imaged within 30-40 minutes. We observed extensive overlap between V-ATPase-a1p(N) and FM4-64 (~34%±11), suggesting association with an endosomal compartment **(Figure 3G-I)**. To pursue this idea, we co-expressed fluorescently-tagged alleles of V-ATPase-a1p(N) and Rab7, a late endosomal marker (82, 83). Most Rab7-positive puncta (~88%±3.2) also contained V-ATPase-a1p(N) **(Figure S4A)**. In contrast, V-ATPase-a1p(N) showed little colocalization with

Lysotracker **(Figure S4B)**. Collectively, the findings support the idea that V-ATPase-a1p is associated with a late endosomal compartment distinct from lysosomes.

VPS8a is necessary for efficient delivery of V-ATPase-a1p to mature mucocyst

The delivery of mucocyst cargo via an endosomal route requires the activity of a specialized CORVET complex, including its *VPS8a* subunit (31). In cells lacking *VPS8a*, the GRL and GRT proteins that in wildtype cells are delivered to mucocysts instead accumulate separately from one another. If delivery of V-ATPase-a1p to mucocysts is via endosomes, it may mis-localize together with GRT proteins in cells lacking *VPS8a*. To test this idea, we imaged V-ATPase-a1p in *Δvps8a* cells **(Figure 4A-H**). We replaced the *VPS8a* gene with a *CHX* drug resistance cassette and confirmed the complete deletion of the *VPS8a* gene by RT-PCR **(Figure 4A-B)**. Using this strain, we imaged endogenously-tagged Grl3p-mCherry with V-ATPase-a1p(G) in wild-type as well as in the *Δvps8a* cells **(Figure 4C-D, inset)**. In wild-type cells, both Grl3p and V-ATPase-a1p(G) accumulate in cortical docked mucocysts (Manders' Coefficients 0.60± SD 0.10). In *Δvps8a* cells, the two proteins only show ~20% co-localization (Manders' Coefficients 0.12± SD 0.05) compared to wildtype cells, strongly suggesting that V-ATPase-a1p(G) is preferentially associated with vesicles that do not contain Grl3p **(Figure 4C-D)**. We therefore asked whether these V-ATPase-a1-positive structures instead contain GRT proteins. In wild-type cells, V-ATPase-a1p(G) accumulates with Grt1p in docked mature mucocysts **(Figure 4E, top panel)**. In *Δvps8a* cells, which lack mature mucocysts, there is roughly 40% overlap between V-ATPase-a1p(G) and Grt1p in non-cortical compartments **(Figure 4E, lower panel and 4F)**. While this is a significant overlap, a majority of the V-ATPase-a1p(G) did not co-localize with Grt1p and must be present in other compartments in *Δvps8a* cells **(Figure 4E–F)**. Consistent with this idea, the fraction of V-ATPase-a1p(G) found in endosomal FM4-64-positive vesicles was 2.5-fold higher in *Δvps8a* cells relative to wildtype **(Figure 4G-H)**. These endosomal vesicles may represent stalled transport intermediates in mucocyst biogenesis.

V-ATPase-a1 is required for secretion from mucocysts

To ask if *V-ATPase-a1* were required for mucocyst biogenesis, we subcloned the 5'UTR and 3'UTR of the *V-ATPase-a1* gene into a pNeo4 knockout vector and transformed it into *Tetrahymena* by biolistic transformation to target the *V-ATPase-a1* gene for disruption via homologous recombination with a drug-resistance cassette. (**Figure 5A)**. During ~3-4 weeks of selection, all ∼45 copies of a gene in the polyploid macronucleus can be replaced with the cassette, resulting in a functional knockout if the gene is not nonessential (77). After generating the *V-ATPase-a1* knockout line, called Δ*v-atpase-a1*, we used reverse transcription PCR (RT-PCR) to detect the gene transcript. The *V-ATPase-a1* transcript was not found in the deletion line (**Figure 5B**), which grew at wildtype rates under standard laboratory conditions. Hence the gene can be considered nonessential.

Since mucocysts are secretory organelles, defects in mucocyst biogenesis would result in reduced mucocyst content secretion. We therefore tested the exocytic response of the knockout cell line using an assay in which brief exposure of wild-type cells to the calcium ionophore dibucaine triggers simultaneous secretion from the several thousand mucocysts per cell (32, 37, 84). We found that *Δv-atpase-a1* cells were grossly deficient in mucocyst content release **(Figure 5C)**, indicating the cells had defects in mucocyst formation and/or exocytosis.

V-ATPase-a1 is essential for mucocyst formation

To test whether *V-ATPase-a1* was required for mucocyst formation per se, we visualized mucocysts by immunofluorescence using two monoclonal antibodies (mAbs) that recognize, respectively, members of the two major families of mucocyst cargo proteins. Grl3p, recognized by mAb 5E9, belongs to the Grl family (32, 37, 39). The second protein, Grt1p, is recognized

by mAb 4D11 (32, 37). Wild-type cells, stained with either the anti-Grl3p or anti-Grt1p mAb, reveal that virtually all mucocysts are docked at the cell periphery, as seen in cell cross sections **(Figure 6Ai, iii and inset)**. In contrast, in *Δv-atpase-a1* cells both mucocyst cargo proteins were relatively sparse, and no docked mucocysts were found at the cell cortex (**Figure 6Aii and iv)**. Notably, a large fraction of the Grl3p and Grt1p in the *Δv-atpase-a1* cells is localized at some distance from the cell cortex (**Figure 6Aii and iv)**, in structures that may represent stalled mucocyst biosynthetic intermediates. *V-ATPase-a1* therefore plays a key role in mucocyst formation. To further confirm it, we examined the morphology of mucocysts in wild-type and *Δv-atpase-a1* cells **(Figure 6B, S5)** by electron microscopy. In wild-type cells, both intermediates or immature mucocysts, as well as mature mucocysts docked at the cell cortex, were detected **(Figure 6B, i and ii)**. However, in the *Δv-atpase-a1* mutant, only intermediates or immature mucocysts were observed **(Figure 6B, iii and S5)**, consistent with the IF results **(Figure 6A)**.

V-ATPase-a1p is required for the processing of pro-Grl proteins

The dense lumenal proteinaceous core of mucocysts in wild-type cells is composed of GRL proteins, and the formation of the mucocyst core depends upon their proteolytic processing during a process of mucocyst maturation (37, 85). The morphologically aberrant mucocysts in *Δv-atpase-a1* cells may be caused by defective processing of Grl proteins **(Figure 6A-B**). Therefore, we asked whether *V-ATPase-a1* was required for the processing of Grl proproteins to their mature forms. We analysed whole-cell lysates of the *Δv-atpase-a1* cells by Western blotting using anti-Grl antisera **(Figure 6C-D)**. In the mutant cells, the Grl proteins were found to accumulate as unprocessed precursors or processing intermediates rather than the fully mature forms found in wild-type cells **(Figure 6C-D)**. This result indicates that the V-ATPase-a1p is required for the processing of pro-Grl proteins.

Mucocysts are not acidic in *Tetrahymena*

We previously found that the key protease responsible for proGrl cleavage, called Cth3p, is related to lysosomal enzymes (32), and might be expected to be most active under acidic conditions. Since V-ATPases are ATP-dependent proton pumps that can acidify compartments, we speculated that the proGrl processing defect in Δ*v-atpase-a1* cells might be due at least in part to a failure to acidify the maturing mucocysts and thereby activate the processing enzymes. To examine this idea, we first asked whether mucocysts are acidic. First, we incubated cells expressing Igr1p-mCherry with Acridine orange (AO) dye, which accumulates in acidic vesicles (86). There was no visible accumulation of AO at sites expected for docked mature mucocysts **(Figure 7A)**. To substantiate this result, we incubated cells expressing Grl3p-mCherry with an alternative probe for acidic compartments, Protonex Green (87). Again, we observed no significant accumulation of Protonex Green in either docked mature mucocysts or in the non-cortical Grl3p-positive puncta, which may be mucocyst biosynthetic intermediates **(Figure 7B)**.

Given the significance of these conclusions for interpreting the role of V-ATPase-a1, we took a third approach to analyzing the pH of mucocysts by endogenously tagging Grl3p with either mEGFP or the super ecliptic pHluorin (SEP) variant, a green fluorescent protein whose emission is relatively quenched at acidic pH. In mammalian cells in which SEP is targeted to the lumen of acidified secretory vesicles, SEP emits bright fluorescence only after the vesicles undergo exocytosis, when their contents become neutralized (88–90). In *Tetrahymena*, we first confirmed the expression of the fusion proteins Grl3p-mEGFP and Grl3p-pHluorin by western blotting using anti-GFP mAb **(Figure 7C)**. Importantly, by confocal microscopy we detected strong fluorescence signals for both Grl3p-mEGFP and Grl3p-pHluorin in non-cortical mucocyst intermediates as well as docked mucocysts **(Figure 7D)**. Taken together, our results strongly suggest that mucocysts are not stably acidified. This conclusion is consistent with

reports that trichocysts of *Paramecium*, which can be considered homologous organelles to *Tetrahymena* mucocysts, are not markedly acidic (86, 91).

The holo-V-ATPase complex is not formed in the mucocyst compartment

The data presented above are consistent with the idea that the mucocyst-associated V-ATPase-a1 subunit might be playing a role distinct from the canonical acidification role of the holo-complex. One question was whether the entire V-ATPase complex is present in mucocysts, or whether some subunits required for proton translocation might be missing. To avoid the potential ambiguities that arise from studying genes that have paralogous copies, we focused on V-ATPase subunits encoded by single genes in *T. thermophila*. To begin, we used multiple approaches including BLAST and structural homology to identify V-ATPase subunits. We discovered that multiple V_1 domain subunits, including VMA1p (subunit-A) and VMA8p (subunit-D) and VMA10p (subunit-G) are expressed as single genes **(Table S3 and Figure S6)**.

Via BLAST searches, three *T. thermophila* candidates for VMA subunits (VMA1p, VMA8p and VMA10p) were found to have high sequence identity with VMA subunits in the Opisthokont *S. cerevisiae*, consistent with widespread conservation of these genes throughout eukaryotes **(Table S3, Figure S6)**. Consistent with the high degree of sequence identity, the predicted structure of VMA8p and VMA1p by Phyre2 revealed high structural similarity with subunit-D and subunit-A of the V_1 domain of mammalian cells, respectively **(Figure S6A and S6B)**. *T. thermophila* VMA10p also showed predicted structural similarity to a V-ATPase subunit in *S. cerevisiae*, subunit-G, though this was more limited 62% coverage and 28% structural identity **(Figure S6C)**. The predicted structural similarities between *T. thermophila* and human V-ATPase subunits were also supported by AlphaFold predictions, for subunit-D (**Figure S6D)** and subunit-A (**Figure S6E)** of *T. thermophila* (green) and human (blue). Taken together, these sequence and structural similarities strongly argue that these genes in *T. thermophila* encode components of a proton-translocating V-ATPase complex.

For each of these three V-ATPase subunits in *Tetrahymena*, each encoded by a single gene without paralogs, we then asked whether they were present in mucocysts. We imaged cells that endogenously co-expressed mCherry-tagged mucocyst marker Grl3p with mNeon-tagged VMA1p, VMA8p and VMA10p, and measured co-localization using the BIOP JACoP plugin **(Figure 8A)**. We found negligible overlap between the VMA subunits and Grl3p at the cell cortex, where mature mucocysts are located **(Figure 8B-D, right panel and 8E)**. This was in striking contrast to the complete overlap between Grl3p and V-ATPase-a1 at the cell cortex **(Figure 8E, 8G and 3D)**. Strikingly, there was instead significant overlap between Grl3p and the VMA subunits deeper in the cytoplasm, at puncta that are likely to include mucocyst biosynthetic intermediates **(Figure 8B-D, left panel, 8F)**.

Taken together, these results argue that multiple V-ATPase subunits, known to form part of the enzymatically-active holo-V-ATPase complex, are present in immature mucocysts. However, only a subset of those subunits persist in mature mucocysts docked at the cell surface. These results suggest that disassembly of the V-ATPase complex occurs during mucocyst maturation. The incompleteness of the V-ATPase complex present in mature mucocysts may explain why these organelles do not maintain an acidic luminal environment.

***V-ATPase-a1* is necessary for a key membrane trafficking step in mucocyst formation**

The results presented above argue that the requirement for V-ATPase-a1 in mucocyst biogenesis cannot be explained by a requirement for stable acidification during mucocyst maturation. We therefore sought to better understand the step(s) at which mucocyst formation is blocked in the absence of V-ATPase-a1. In addition to proteolytic maturation of Grl proproteins, a well-documented step in mucocyst formation is heterotypic vesicle fusion that brings together the Grl proteins, which may be trafficked directly from the TGN, with Grt

proteins as well as at least some of the key processing enzymes like Cth3p, which appear to be trafficked via endosomes. This fusion step involves a Syntaxin 7-like homolog, Stx7l1 and the CORVET subunit Vps8a (31). Stx7l1p itself, but not VPS8ap, remains associated with mature mucocysts. In cells lacking either *VPS8a* or *Stx7l1*, Grl and Grt proteins accumulate in separate vesicles, and mature mucocysts are not formed.

To test whether V-ATPase-a1 is required for this key step of heterotypic vesicle fusion, we used indirect immunofluorescence in fixed cells to localize Grt1p with Grl1p and Stx7l1p. These cargo proteins, Grl1p and Grt1p, accumulate exclusively in fully docked mature mucocysts in wild-type cells **(Figure 9A, top panel)**. In contrast, in *Δv-atpase-a1* cells, both cargo proteins accumulate in a heterogeneous cohort of aberrant cytoplasmic vesicles **(Figure 9A, middle panel)**. In comparison to wild-type cells, Grl1p and Grt1p show significantly less co-localization (~51%) in *Δv-atpase-a1* **(Figure 9B)**, which is similar to their level of co-localization in *Δvps8a cells* **(Figure 9A, lower panel and 9B)**. Consistent with previous results, Stx7l1p-GFP co-localizes with Grt1p in wild-type cells, both present in docked mucocysts **(Figure 9C, top panel and S7A)**. That co-localization is ~68% reduced in *Δv-atpase-a1* cells **(Figure 9C-D)**. Notably, a greater extent of co-localization is observed in the mutant cells between Grl3p and Stx7l1p **(Figure S7B-C)**. These results are consistent with earlier reports that Stx7l1p is associated with vesicles containing Grl3p rather than Grt1p (21, 31). Our results suggest that the absence of V-ATPase-a1 blocks efficient heterotypic fusion between Grl- and Grt-containing vesicles.

We previously provided evidence for a model in which the delivery of Grt1p depends on its interaction with a VPS10-family receptor, Sor4p (11). That model would predict that the Grt1p-containing vesicles in Δ*v-atpase-a1* cells, if they are stalled biosynthetic intermediates, should also contain Sor4p. In agreement with this model, we found that the co-localization of Grt1p and Sor4p increased 3.5-fold in the Δ*v-atpase-a1* mutant compared to in wildtype cells **(Figure 9E-F, S8)**. Taken together, our results support the idea that V-ATPase-a1p promotes fusion of Grl1p-containing and Sor4p/Grt1-containing vesicles during mucocyst formation.

Our prior studies also provided indirect evidence that delivery of Cth3p to mucocysts might, like Grt1p, depend on Sor4p-dependent trafficking through endosomes (31). Cth3p in the Δ*v-atpase-a1* mutant might therefore behave equivalently to Grt1p, e.g., co-localize in the same puncta. However, we instead found that endogenously-tagged Cth3p was virtually undetectable when expressed in the Δ*v-atpase-a1* background **(Figure S9A)**. Consistent with this imaging, Western blotting showed that the mutant cells accumulated much lower levels of Cth3p-GFP compared to wildtype cells **(Figure S9B-C)**. This result suggests that in the absence of V-ATPase-a1p, Cth3p trafficking is altered in a way that results in either its rapid secretion from the cell, or its degradation, since the wildtype and mutant cells had comparable levels of the CTH3-GFP transcript **(Figure S9D)**. This difference between Grt1p and Cth3p may be related to a large quantitative difference in their relative reliance on Sor4p-dependent sorting, consistent with the idea that Cth3p follows a more complex itinerary in the endomembrane network (11, 32). Based on these data, we proposed a model for the mucocyst biogenesis pathway in *T. thermophila* **(Figure 10)**, extending the model proposed by Sparvoli *et al*, 2018.

Discussion

In *Tetrahymena thermophila*, the biogenesis of secretory vesicles known as mucocysts has previously been shown to depend on a set of proteins associated in other lineages with LROs (21, 31). Here, we investigated whether a V-ATPase was also required for mucocyst formation. Based on genome analysis, *T. thermophila* is likely to contain a surprisingly large number of distinct and compartment-specific V-ATPases for a unicellular organism, a phenomenon previously investigated for a somewhat related ciliate, *Paramecium tetraurelia* (92–94). In

other organisms, the localization specificity of V-ATPases has been shown to depend on determinants in the a-subunit of the V_o subcomplex (41, 65, 68–71, 95, 96). Consistent with this idea, in animal cells distinct a-subunits are found respectively in coated vesicles, the Golgi apparatus/early endosomes, and late endosomes/lysosomes (40, 41, 66, 69). In *T. thermophila*, we discovered six genes encoding a-subunits of the V-ATPase, as opposed to the four a-subunit genes in mammals (41, 68) while 17 a-subunit genes have been described in another ciliate, *Paramecium tetraurelia* (92). In *Paramecium*, these seventeen genes could be divided into nine families and localized to at least seven different compartments. Of these, only the a3 subunit in *Paramecium* was implicated in the formation of trichocysts, which are organelles homologous to mucocysts. Silencing the a3 subunit impaired both exocytosis and trichocyst formation (92). We found a similar result in the knockout a1 subunit in *Tetrahymena*. However, the role of the a3 subunit in trichocyst formation and trafficking is yet unknown.

Among a total of 6 *T. thermophila* paralogs encoding a-subunits of the V_o subcomplex, we discovered that one of them is transcriptionally coregulated with known mucocyst-associated genes, and that the corresponding protein localizes strongly to mature docked mucocysts as well as to Rab7-positive puncta. *Tetrahymena*, Rab7 was previously shown to be present on vesicles containing the mucocyst-destined protein Grt1p (31). Consistent with this, we found significant colocalization between V-ATPase-a1p and Grt1p in cytoplasmic puncta, i.e., not mature mucocysts, but potentially intermediates in mucocyst biogenesis.

The association of V-ATPase with Rab7 has been reported in other cell types. Studies in osteoclasts demonstrated that subunit a3 recruits Rab7 to secretory lysosomes, promoting their transport to the cell periphery where they deliver bone-resorbing enzymes together with the proton pump. This finding and earlier research indicate that V-ATPase has both enzymatic and non-enzymatic roles in osteoclasts: acidifying bone resorption lacunae and directing organelle transport (69, 73). Similarly, in neurons V-ATPase plays roles in the interconnected functions of acidification and exocytosis (97).

Next, we tested whether *V-ATPase-a1* gene was required for mucocyst formation. The *V-ATPase-a1* disruption strain showed defects in both mucocyst biogenesis and exocytosis. We previously demonstrated such defects in cells that had the *CTH3* gene disrupted, which is a key processing enzyme in *Tetrahymena* (32). This result is consistent with the idea that V-ATPase-a1p may be directly or indirectly required for Cth3p activity since the V-ATPase complex generates an acidic environment for the activation of processing enzymes in animal cells.

The primary function of the V-ATPase is to transport H^+ ions and generate acidic environments in various intracellular vesicles and organelles, which are required for many important cell biological events to occur. For example, in animal cells, the acidic environment of DCGs activates processing enzymes (98, 99). Remarkably, the V-ATPase complex subunits in ciliates are found on LROs and contractile vacuole complex (CVC) but does not acidify them. For instance, the CVC lumen is not detectably acidified (100, 101). A similar finding was reported in *Dictyostelium* (102). Previously, non-acidic endolysosome-related organelles (ELROs) were found in neuronal and keratinocyte cells that lack acid hydrolases (103–106). In *Paramecium* cells, secretory granules are not acidic compartment (86, 91). Thus, it has been postulated that the proton gradients produced by these pumps are used to generate coupled gradients of other ions (102, 107, 108).

However, the physiological regulation of the V-ATPase in mammalian cells is still poorly known. In yeast and mammalian cells, the reversible assembly and disassembly of the V-ATPase V_1 and V_o domains regulates endolysosomal/lysosomal pH (60, 109). We found that the V-ATPase subunits (VMA1p, VMA8p and VMA10p) in *Tetrahymena*, which are subunits of V_1 domains A, D and G, respectively, are not present in mature, docked mucocysts, but they instead are found at significant levels in a pool of cytoplasmic puncta that are likely to represent

immature mucocysts, since they contain the mucocyst cargo protein Grl3p. These results suggest that the mucocyst-associated V-ATPase complex disassembles during maturation, with only a subset of the subunits remaining mucocyst-associated, which is correspondingly non-acidic. Importantly, at least one of the dissociated subunits, VMA8, has previously been shown to be essential for coupling of proton transport and ATP hydrolysis in yeast(110, 111). Therefore, the remnant V-ATPase complex in mature mucocysts is likely to be disabled for proton translocation, which can explain why mucocysts do not maintain an acidic luminal environment. Although non-acidic storage LROs are not unique to ciliates, similar phenomena of V-ATPase disassembly could be an important feature of animal LROs.

Most of the fusion in eukaryotes is mediated by SNAREs and their cofactors (112). Several lines of evidence have recently emerged indicating that V-ATPase may play a role in membrane fusion events by producing electrochemical gradients or as a structural component of the fusion machinery (113, 114). For example, yeast lysosomal vacuoles and VopQ, a type III effector released by *Vibrio parahaemolyticus*, bind to V-ATPase, inhibiting its activity and preventing fusion (114). The complexity of the V-ATPase structure makes it difficult to determine how V-ATPase would function in fusion. However, several lines of evidence also suggest that V-ATPase-a subunit isoforms have a role in the trafficking of several components of LROs and secretory pathways (46, 69, 73, 113, 115). For example, the lysosomal a3 isoform of V-ATPase is necessary for the transport of Mon1A-Ccz1, a guanine nucleotide exchange factor (GEF) for Rab7, to secretory lysosomes (73). Also, screening in *Drosophila* revealed that a mutation in the V_0 subunit V_{100}, which binds to Syntaxin and inhibits its activity, caused neurotransmission and trafficking defects (116, 117). Therefore, we propose to test this function in *Tetrahymena* by monitoring the trafficking of cargo proteins Grl1p and Grt1p. In wild-type cells, both cargo proteins are found at the cell cortex alongside docked mature mucocysts. In contrast, in *Δv-atpase-a1* cells, vesicles fail to dock at the cell cortex. Interestingly, in Δ*v-atpase-a1* cells, a significant amount of Gr1p and Grt1p remain in the distinct compartments, indicating that vesicles do not undergo homotypic or heterotypic fusion that occurs during normal mucocyst development. We also tested other candidates of mucocysts, Stx7l1p, associated with Grl3p containing vesicles and not fused with Grt1p containing vesicles in Δ*vps8a* (21). In *Δv-atpase-a1* cells, the majority of Stx7l1p is not fused with Grt1-containing vesicles, indicating that V-ATPase is necessary to convey GRL family members to a secretory compartment containing GRT proteins. In addition, the mucocyst sorting receptor Sor4p and other cargo proteins, such as Grt1p, which is delivered to immature mucocysts in wild-type cells, are found in vesicles that are accumulated in *Δv-atpase-a1* cells. These vesicles are most likely transient intermediates in mucocyst formation that accumulate in the mutant *Δv-atpase-a1* because their ability to fuse and tether with their target is inhibited. Interestingly, another mucocyst protein, Cth3p, is almost absent in Δ*v-atpase-a1* cells. However, our result does not indicate whether V-ATPase-a1p is directly or indirectly implicated in Cth3p trafficking. Based on these findings, we conclude that V-ATPase-a1p is required for efficient delivery of mucocyst proteins to promote homo/heterotypic fusion either directly or indirectly.

Materials And Methods

Reagents, *Tetrahymena* Strains and culture conditions

Tetrahymena thermophila strains were grown overnight at 30°C with agitation in nutrient rich SPP medium (2% proteose peptone, 0.2% dextrose, 0.1% yeast extract, 0.003% ferric EDTA) supplemented with 250 μg/ml streptomycin sulfate, 250 μg/ml penicillin G, and 0.25 μg/ml amphotericin B fungizone, to medium density (2-3 × 10^5 cells/ml). Cu428 wild type strain was used as a control for all experiments and for biolistic transformation. 10mM Tris buffer (pH

7.4) was used for washing cells and as a starvation medium to reduce autofluorescence in food vacuoles. Cell culture densities were measured using a hemocytometer. *T. thermophila* strains used in this study are listed in **Table 1**. All reagents, chemicals, plasmids, and other information are listed in Key Resources Supplemental **Table S4**. The constructs p2xHA-3xmCherry-Rab7p-NCVB, pGrl3p-GFP-CHX, pSor4p-GFP-CHX, p-2xmNeon-6c-myc-Neo4, p3xmCherry-2xHA-Neo4, pCth3p-mEGFP-CHX, and *Δvps8a*-Neo4 were from (31); pmEGFP-Neo4 and pNeo4 KO vector were from (32); pStx7l1p-GFP-Blasticidin was from (21). Wild type strains Cu428 and pPur4 vector were generously provided by Dr Abdur Rahaman (NISER, India) and Kazufumi Mochizuki (University of Montpellier, France), respectively.

Table 1: *Tetrahymena* Strains used in this study

Strain name	Phenotype	Details of relevant genetic modification	Source
Cu428	Wild type	None	Dr Abdur Rahaman (NISER, India)
Igr1p-3xmCherry-2xHA	Endogenous-level expression of 3xmCherry-2xHA-tagged Igr1p	C-terminal fusion of Igr1p and 3xmCherry-2xHA with Pur4 cassette, integrated at the macronuclear *IGR1* locus	(118)
SKBN001	*Δv-atpase-a1;* no detectible *V-ATPase-a1* expression	Replaces nucleotides 1 to 3479 bp of macronuclear V-ATPase-a1 ORF with Neo4 cassette.	This study
SKBN002	Endogenous-level expression of 2xmNeon-6xc-myc-tagged V-ATPase-a1p [V-ATPase-a1p(N)] N: Neon	C-terminal fusion of V-ATPase-a1p and 2xmNeon-6xc-myc with Neo4 cassette, integrated at the macronuclear *V-ATPase-a1* locus	This study
SKBN003	Endogenous-level expression of GFP-tagged V-ATPase-a1p [V-ATPase-a1p(G)] G: GFP	C-terminal fusion of V-ATPase-a1p and GFP with Neo4 cassette, integrated at the macronuclear *V-ATPase-a1* locus	This study
SKBN004	Endogenous-level expression of 3xmCherry-2xHA-tagged Grl3p	C-terminal fusion of Grl3p and 3xmCherry-2xHA with Pur4 cassette, integrated at the macronuclear *GRL3* locus	This study
SKBN005	Endogenous-level expression of 2xmNeon-6xc-myc-tagged V-ATPase-a1p [V-ATPase-a1p(N)] and 3xmCherry-2xHA-tagged Grl3p	C-terminal fusion of V-ATPase-a1p and 2xmNeon-6xc-myc with Neo4 cassette, integrated at the macronuclear *V-ATPase-a1* locus. Also, C-terminal fusion of Grl3p and 3xmCherry-2xHA with Pur4 cassette, integrated at the macronuclear *GRL3* locus	This study
SKBN006	Endogenous-level expression of 2xmNeon-6xc-myc-tagged V-ATPase-a1p [V-ATPase-a1p(N)] and 3xmCherry-2xHA-tagged Igr1p	C-terminal fusion of V-ATPase-a1p and 2xmNeon-6xc-myc with Neo4 cassette, integrated at the macronuclear *V-ATPase-a1* locus. Also, C-terminal fusion of Igr1p and 3xmCherry-2xHA with Pur4 cassette, integrated at the macronuclear *IGR1* locus	This study
SKBN007	Endogenous-level expression of 2xmNeon-6xc-myc-tagged	C-terminal fusion of V-ATPase-a1p and 2xmNeon-6xc-myc with Neo4 cassette, integrated at the macronuclear *V-ATPase-*	This study

	V-ATPase-a1p [V-ATPase-a1p(N)]. Inducible expression of 2xHA-3xmCherry-tagged Rab7p	*a1* locus. Also, N-terminal fusion of Rab7p and 2xHA-3xmCherry, expressed under the control of the *MTT1* promoter, at the macronuclear *MTT1* locus.	
SKBN008	Endogenous-level expression of GFP-tagged V-ATPase-a1p [V-ATPase-a1p(G)] and 3xmCherry-2xHA-tagged Grl3p	C-terminal fusion of V-ATPase-a1p and GFP with Neo4 cassette, integrated at the macronuclear *V-ATPase-a1* locus. Also, C-terminal fusion of Grl3p and 3xmCherry-2xHA with Pur4 cassette, integrated at the macronuclear *GRL3* locus	This study
SKBN009	Endogenous-level expression of GFP-tagged V-ATPase-a1p [V-ATPase-a1p(G)] and 3xmCherry-2xHA-tagged Grl3p. *Δvps8a;* no detectible *VPS8a* expression	C-terminal fusion of V-ATPase-a1p and GFP with Neo4 cassette, integrated at the macronuclear *V-ATPase-a1* locus. Also, C-terminal fusion of Grl3p and 3xmCherry-2xHA with Pur4 cassette, integrated at the macronuclear *GRL3* locus. Replaced whole gene, -34 bp upstream and 22 bp downstream of *VPS8a* in macronuclear with CHX cassette.	This study
SKBN0010	Endogenous-level expression of 2xmNeon-6xc-myc-tagged V-ATPase-a2p and 3xmCherry-2xHA-tagged Grl3p	C-terminal fusion of V-ATPase-a2p and 2xmNeon-6xc-myc with Neo4 cassette, integrated at the macronuclear *V-ATPase-a2* locus. Also, C-terminal fusion of Grl3p and 3xmCherry-2xHA with Pur4 cassette, integrated at the macronuclear *GRL3* locus	This study
SKBN0011	Endogenous-level expression of GFP-tagged Cth3p and 3xmCherry-2xHA-tagged Grl3p	C-terminal fusion of Cth3p and GFP with CHX cassette, integrated at the macronuclear *CTH3* locus. Also, C-terminal fusion of Grl3p and 3xmCherry-2xHA with Pur4 cassette, integrated at the macronuclear *GRL3* locus	This study
SKBN0012	Endogenous-level expression of GFP-tagged Cth3p and 3xmCherry-2xHA-tagged Grl3p. *Δv-atpase-a1;* no detectible *V-ATPase-a1* expression.	C-terminal fusion of Cth3p and GFP with CHX cassette, integrated at the macronuclear *CTH3* locus. Also, C-terminal fusion of Grl3p and 3xmCherry-2xHA with Pur4 cassette, integrated at the macronuclear *GRL3* locus. Replaces nucleotides 1 to 3479 bp of macronuclear V-ATPase-a1 ORF with Neo4 cassette.	This study
SKBN0013	Endogenous-level expression of GFP-tagged Grl3p	C-terminal fusion of Grl3p and GFP with Neo4 cassette, integrated at the macronuclear *GRL3* locus	This study
SKBN0014	Endogenous-level expression of pHluorin-tagged Grl3p	C-terminal fusion of Grl3p and pHluorin with Neo4 cassette, integrated at the macronuclear *GRL3* locus	This study
SKBN0015	Endogenous-level expression of GFP-tagged Sor4p.	C-terminal fusion of Sor4p and GFP with CHX cassette, integrated at the macronuclear *SOR4* locus.	This study
SKBN0016	Endogenous-level expression of GFP-tagged	C-terminal fusion of Sor4p and GFP with CHX cassette, integrated at the	This study

	Sor4p. *Δv-atpase-a1;* no detectible *V-ATPase-a1* expression.	macronuclear *SOR4* locus. Replaces nucleotides 1 to 3479 bp of macronuclear V-ATPase-a1 ORF with Neo4 cassette.	
SKBN0017	Endogenous-level expression of 2xmNeon-6xc-myc-tagged VMA1p and 3xmCherry-2xHA-tagged Grl3p	C-terminal fusion of VMA1p and 2xmNeon-6xc-myc with Neo4 cassette, integrated at the macronuclear *VMA1* locus. Also, C-terminal fusion of Grl3p and 3xmCherry-2xHA with Pur4 cassette, integrated at the macronuclear *GRL3* locus	This study
SKBN0018	Endogenous-level expression of 2xmNeon-6xc-myc-tagged VMA8p and 3xmCherry-2xHA-tagged Grl3p	C-terminal fusion of VMA8p and 2xmNeon-6xc-myc with Neo4 cassette, integrated at the macronuclear *VMA8* locus. Also, C-terminal fusion of Grl3p and 3xmCherry-2xHA with Pur4 cassette, integrated at the macronuclear *GRL3* locus	This study
SKBN0019	Endogenous-level expression of 2xmNeon-6xc-myc-tagged VMA10p and 3xmCherry-2xHA-tagged Grl3p	C-terminal fusion of VMA10p and 2xmNeon-6xc-myc with Neo4 cassette, integrated at the macronuclear *VMA10* locus. Also, C-terminal fusion of Grl3p and 3xmCherry-2xHA with Pur4 cassette, integrated at the macronuclear *GRL3* locus	This study
SKBN0020	Inducible expression of GFP-tagged Stx7l1p.	C-terminal fusion of Stx7l1p and GFP with BLAS cassette, integrated at the macronuclear *MTT1* locus.	This study
SKBN0021	Inducible expression of GFP-tagged Stx7l1p. *Δv-atpase-a1;* no detectible *V-ATPase-a1* expression.	C-terminal fusion of Xtx7l1p and GFP with BLAS cassette, integrated at the macronuclear *MTT1* locus. Replaces nucleotides 1 to 3479 bp of macronuclear V-ATPase-a1 ORF with Neo4 cassette.	This study

Exocytosis assay

Exocytosis was stimulated by dibucaine as described previously (32, 119).

Verification of knockouts of genes by reverse transcriptase (RT)-PCR

RT-PCR was performed as described previously (32). Briefly, total RNA was extracted by following the manufacturer's instructions using RNeasy mini spin column kits (Qiagen, USA). cDNA (200-500 base pairs of each gene) was synthesized and further amplified using the one step RT-PCR kit (Qiagen USA,) as per manufacturer's protocol using primers designated in **Supplemental Table S2**. To provide positive controls, RT-PCR using β-tubulin specific primers were performed in parallel.

Biolistic transformation

Biolistic transformations were carried out as described (32, 39) with some modifications. Briefly, cells were grown in SPP medium and incubated at 30°C with swirling to reach medium cell density. The next day, cells were washed twice with 10 mM Tris pH 7.4 and starved in the same buffer for 16 to 18 hours. 15 μg of total linearized plasmid DNA were conjugated with 0.6 μ gold particles (Bio-Rad, USA) as per the manufacturer's instructions. Four hours after bombardment, drugs were added to cultures that were swirling at 30°C to select positive transformants. Positive transformants were identified after 3–4 days and serially transferred 5 days/week in increasing concentrations of drug and decreasing concentrations of $CdCl_2$ (up to

6.5 mg/ml of paromomycin, 0.1 μg/ml $CdCl_2$; up to 200 μg/ml of puromycin and 0.5 μg/ml $CdCl_2$; up to 60 μg/ml of blasticidin and 0.5 μg/ml $CdCl_2$, 20 μg/ml of cycloheximide and 0.8 μg/ml $CdCl_2$) for 4-5 weeks before further testing. Each line was evaluated using at least three independent transformants.

Generation of *V-ATPase-a1* and *VPS8a* knockout strains

Upstream (~1 kb) and downstream (~1 kb) regions of the *V-ATPase-a1* (TTHERM_01332070) gene were amplified by PCR and subcloned into the SacI and XhoI sites of the pNeo4 vector, respectively, using the In-Fusion cloning kit (TaKaRa, Japan). *V-ATPase-a1* knockout construct was linearized using KpnI and SapI enzymes before biolistic transformation into Cu428 cells. *Δvps8a-CHX* construct was used to disrupt the *VPS8a* (TTHERM_00290710) gene. For this, the cycloheximide-resistance *(CHX)* sequence from Grl3p-3xmCherry-CHX construct was PCR amplified and used to replace Neo4 in *Δvps8a*-Neo4 at PstI and NheI sites using In-fusion cloning. The construct was linearized with KpnI and SacI and biolistically transformed into cells co-expressing GFP-tagged V-ATPase-a1p and 3xmCherry-tagged Grl3p at the *V-ATPase-a1* and *GRL3* loci, respectively. The ORF intervals deleted for each targeted gene were: *V-ATPase-a1* 1 to 3479 bp (whole gene); and -34 bp to +22 bp of *VPS8a* (whole gene, -34 bp upstream and 22 bp downstream of *VPS8a*). The primers used to amplify target regions are listed in **Supplemental Table S2**.

Live-cell microscopy

Cultures for live microscopy were analyzed at mid-density unless otherwise indicated. To image cells expressing mNeon, mCherry, GFP or pHluorin-tagged fusion proteins, transformants were cultured overnight in SPP media and then transferred into 10 mM Tris pH 7.4 for 2-4 h to reduce autofluorescence in food vacuoles. Co-localization in live cells was determined by simultaneous imaging of mNeon or GFP-tagged fusion proteins with mCherry-tagged mucocyst markers. To simultaneously localize mNeon tagged V-ATPase-a1p [V-ATPase-a1p(N)] with Lyso-Tracker Red (Invitrogen, USA), cells were incubated with 200 nM Lyso-Tracker Red for 5 min and images were captured as previously described (32). For co-localization of V-ATPase-a1p(N) and FM4-64 (Invitrogen, USA), cells were treated with 5 μM FM4-64, which labels endosomes, for 5 minutes and then pelleted and resuspended in 10 mM Tris pH 7.4. Subsequently, cells were imaged within 30-40 minutes. For Acridine Orange and Protonex Green staining, cells expressing V-ATPase-a1p(N) were incubated with 0.1μg/ml Acridine Orange (Invitrogen, USA) or 5μM Protonex Green (AAT Bioquest, USA) for 2 min and 120 min, respectively, in the dark. Cells were washed twice with 10 mM Tris pH 7.4 and observed under the microscope. To check co-localization between V-ATPase-a1p(N) and Rab7 positive endosomes, cells were transformed to co-express V-ATPAse-a1p(N) at the endogenous locus with mCherry-Rab7p. Transgene mCherry-Rab7p was induced for 2h in SPP with 2 μg/ml $CdCl_2$ followed by induction with 0.5μg/ml $CdCl_2$ for 2h in starvation buffer 10 mM Tris, pH 7.4. Stx7l1p-GFP was induced with $CdCl_2$ as mentioned above. Live-cell images were captured using an Olympus SR10 spinning disk super-resolution confocal microscope (Olympus, Japan). Both confocal and super-resolution modes with a 60x oil objective were used to capture time-lapse videos. For z sectioning, SORA disk-enabled acquisition was used to keep the z slice step size at 0.3 μm. After removing the background signal from the images, they were saved as JPEGs that were denoised, colored, and adjusted for brightness and contrast using the Fiji application (http://fiji.sc/Fiji).

Immunofluorescence Assay

Cells were grown to reach a cell density of $5x10^5$ cells/ml, then starved in 10 mM Tris pH 7.4 for 2 hours, fixed, and immunolabeled as described previously (32). Monoclonal antibodies

5E9 [1:9; (120) and 4D11 1:5; (121)] were used to visualize Grl3p and Grt1p, respectively followed by goat anti-mouse conjugated with Texas red (1:100; Invitrogen, USA). Grl1p and GFP-tagged fusion proteins were visualized by 1:5000 diluted rabbit anti-GRL1 (118, 122), and rabbit anti-GFP (1:400; (Invitrogen, USA), respectively, followed by anti-rabbit antibody conjugated with Alexa 488 (1:250 Invitrogen, USA). Cells were double immunolabeled with mouse mAb 4D11 and rabbit anti-Grl1 to visualize the fusion of Grl1p and Grt1p-containing vesicles. Fixed cells were imaged on a Leica SP5 II STED-CW super-resolution laser scanning confocal microscope (Leica, Germany) or an Olympus SR10 spinning disk super-resolution confocal microscope. Images were analyzed as described above.

Electron microscopy

Cells were grown to reach high cell density (10^6/ml), washed with 10mM Tris media (pH 7.4), fixed, section stained and imaged as described previously (39).

SDS-PAGE, and Western blotting

Whole cell lysates were prepared from $3x10^5$ cells as described (32). Using mouse anti-c-Myc Agarose beads (Thermo Fisher Scientific, USA), 2xmNeon-6c-myc-tagged fusion proteins were immunoprecipitated from detergent lysates as previously described (31). Samples were separated using SDS-PAGE and then transferred to 0.45µ PVDF membranes (Merck Millipore, USA) for western blots. Blots were blocked and probed with antibodies described previously (85). The primary antibodies rabbit anti-Grl1, rabbit anti-Grl3 (32), mouse monoclonal anti-GFP (Biolegend, USA), mouse monoclonal anti-GFP (Rockland Immunochemicals, USA) and anti-c-Myc (Sigma, USA) were diluted 1:2000, 1:800, 1:5000, 1:1000 and 1:4000, respectively. Proteins was visualized using Super Signal West Femto Maximum Sensitivity Substrate (Thermo Fisher Scientific, USA), and enhanced chemiluminescence horseradish peroxidase–linked anti-rabbit (Bio-Rad, USA), anti-mouse (Bio-Rad, USA),) and anti-mouse for IP (Abcam, UK), with the secondary antibodies diluted 1:5000, 1:5000, and 1:1000, respectively.

Expression of V-ATPase-a1p, V-ATPase-a2p, VMA1p, VMA8p, VMA10p, Cth3p, Grl3p and Igr1p at endogenous locus

The p2xmNeon-6c-myc-Neo4 and pmEGFP-Neo4 vectors were previously described (11, 31, 32). To create pV-ATPase-a1p-2xmNeon-6c-myc-Neo4 and pV-ATPase-a1p-pmEGFP-Neo4, the genomic DNA of V-*ATPase*-a1 (TTHERM_01332070; 1462bp) without stop codon and 1000bp of V-*ATPase*-a1 downstream genomic region were amplified and cloned into p2xmNeon-6c-myc-Neo4 or pmEGFP_Neo4 vectors at NotI and XhoI sites, respectively, using In-Fusion Cloning (TaKaRa, Japan). The construct was named pV-ATPase-a1p-2xmNeon-6c-myc-Neo4 [pV-ATPase-a1p(N). and pV-ATPase-a1p-pmEGFP-Neo4 [pV-ATPase-a1p(G) were linearised with KpnI and SacI, 2xmNeon-6c-myc or monomeric mEGFP were fused to the C-terminus of V-*ATPase*-a1 at the endogenous macronuclear locus via homologous recombination. The similar approach was used to amplify the genomic DNA without stop codon (~700-900bp) and downstream genomic sequence (~600-850bp) of other V-ATPase subunits *V-ATPase-a2* (TTHERM_00463420), *VMA1* (TTHERM_00339640), *VMA8* (TTHERM_00821870) and *VMA10* (TTHERM_00052460) for fusion of 2xmNeon-6c-myc to the C-terminus of V-ATPase subunits at the endogenous macronuclear locus. For the generation of pGrl3p-3xmCherry-2xHA-Pur4, the pGrl3p-GFP-CHX vector was used as template (31). BamHI/SpeI sites were used to replace monomeric mGFP with p3xmCherry-2xHA, while PstI/HindIII sites were used to replace CHX (cycloheximide resistance gene) with Pur4 (puromycin resistance gene) to generate pGrl3p-3xmCherry-2xHA-Pur4 vector. The

pmEGFP-Neo4 and pGrl3p-3xmCherry-2xHA-Pur4 vectors were used to make the pGrl3p-mEGFP-Neo4 construct. The genomic (857 bp excluding stop codon) and downstream sequence (783bp) of *GRL3* gene were excised from pGrl3p-3xmCherry-Pur4 vector using BamHI/ SacI and HindIII/KpnI, respectively and ligated into pmEGFP-Neo4 vector at mentioned sites respectively using T4 DNA ligase (New England, Biolabs, USA). pGrl3p-mEGFP-Neo4 vector was used as template to generate pGrl3p-pHluorin-Neo4 construct. Super ecliptic pHluorin (SEP) variant sequence was derived from the pHluorin MT1-MMP vector (123). The pHluorin gene (lacking stop codon), codon optimised for *Tetrahymena* using the IDT Codon optimization tool, was synthesized (Eurofins Genomics Pvt Ltd) with added BamHI/SpeI sites at 5' and 3' end of gene. Monomeric mGFP from pGrl3p-mEGFP-Neo4 was replaced with pHluorin using BamHI/SpeI sites to generate pGrl3p-pHluorin-Neo4. All constructs were confirmed by DNA sequencing. The final constructs were linearized with SacI and KpnI before transformation. The p2xHA-3xmCherry-RAB7p-NCVB construct was linearized by digestion with SfiI and transformed into cells expressing V-ATPase-a1p(N) by biolistic transformation. pGrl3p-3xmCherry-2xHA-Pur4, pGrl3p-mEGFP-Neo4 and pGrl3p-pHluorin-Neo4 were transformed into wildtype Cu428 using biolistic transformation. V-ATPase-a1p-2xmNeon-6c-myc-Neo4 vector was transformed into Cu428 cell expressing Grl3p-3xmCherry-2xHA-Pur4 or Igr1p-3xmCherry-2xHA-Pur4, while pV-ATPase-a1p-pmEGFP-Neo4, pV-ATPase-a2p-2xmNeon-6c-myc-Neo4, pVMA1p-2xmNeon-6c-myc-Neo4, pVMA8p-2xmNeon-6c-myc-Neo4 and pVMA10p-2xmNeon-6c-myc-Neo4 vectors were transformed into cells expressing Grl3p-3xmCherry-2xHA-pur4. pCth3p-mEGFP-CHX (31) was transformed into wild type and *Δv-atpase-a1* cells expressing Grl3p-3xmCherry-2xHA. The *Δvps8a* construct was transformed into cells co-expressing V-ATPase-a1p(N) and Grl3p-3xmCherry-2xHA-pur4.

Phylogenetic tree construction

Protein BLAST (BLASTp) was used to identify homologs of V- ATPase-a1p (TTHERM_01332070; XP_001010002.1) in ciliates (*Paramecium*), apicomplexans (*Toxoplasma gondii), Arabidopsis thaliana, Caenorhabditis elegans, Drosophila melanogaster, Danio rerio,* and *Homo sapiens*, as shown in Supplemental **Table S1**. For tree construction, the top hits from each lineage were selected, assembled, and aligned using ClustalX (1.8). Phylogenetic trees were built using MEGA 11 software (Molecular Evolutionary Genetics Analysis: www.megasoftware.net/) with the maximum likelihood option, without gap regions and with1000 bootstrap replicates.
he top hits were selected from each lineage

***In silico* analyses**

The transmembrane domains of V-ATPase-a paralogs (a1p-a6p) were obtained from the UniProt database (https://www.uniprot.org). The extent of homology between the corresponding transmembrane domains among the paralogs (i.e., a comparison of a1 to a2-a6) was determined using a Blast search and the UniProt database. Protein sequences of V-ATPase-a subunit paralogs (a1p-a6p) were extracted from TGD (https://tet.ciliate.org/) and aligned using EMBOSS Needle (https://www.ebi.ac.uk/jdispatcher/psa/emboss_needle) using the default parameters. Transcription profiles were downloaded from the Tetrahymena Functional Genomics Database (http://tfgd.ihb.ac.cn) (79–81). For plotting, each profile was normalized by setting the maximum expression level of the gene to 1. The V-ATPase-a1p structure was predicted using Protein Homology/Analogy Recognition Engine V 2.0 (Phyre 2), a web portal for protein modelling (124). Structural homologs of the *T. thermophila* V-ATPase-a1p were identified using the AlphaFold Protein Structure Database (https://alphafold.ebi.ac.uk/).

Acknowledgements

We thank Dr Prasad Abnave (NCCS, Pune) for critical evaluation and valuable feedback on the manuscript and Dr Jomon Joseph for many helpful discussions. We heartily thank our lab members Shubham Yadav, Vandna Maurya and Satya Santoshi for their continuous and generous support; Nikhat Khan for skilful technical assistance in all the above experiments. S.K.'s laboratory is funded by Department of Biotechnology (DBT), Ministry of Science and Technology India (BT/PR38584/MED/122/247/202), Department of Science and Technology (DST), Ministry of Science and Technology India (CRG/2021/000732) and DBT/Wellcome Trust India Alliance (IA/I/22/2/506480). A.P.T. was supported by the National Science Foundation (MCB 1937326). We dedicate this work to our late Director Dr Mohan R. Wani.

Author contributions

Conceptualization, S.K., A.P. and A.P.T; Methodology, A.P., N. T. and D. S.; Data Analysis, S. K. and A. P.; Investigation and experiment S. K., A.P., N. T., D.S., and L.K.B.; Resources, S.K. A.P.T; Writing – Original Draft, S. K.; Writing – Review & Editing, S. K., A.P., D. S. and A.P.T; Visualization, A.P., and N. T.; Supervision, S.K.; Funding Acquisition, S.K.

Declaration of Interests

The authors declare no competing interests.

References:

1. Palade G. 1975. Intracellular aspects of the process of protein synthesis. Science 189:867.

2. Keller P, Simons K. 1997. Post-Golgi biosynthetic trafficking. J Cell Sci 110 (Pt 24):3001–9.

3. Röder P V, Wong X, Hong W, Han W. 2016. Molecular regulation of insulin granule biogenesis and exocytosis. Biochem J 473:2737–56.

4. Orci L, Ravazzola M, Amherdt M, Madsen O, Perrelet A, Vassalli JD, Anderson RGW. 1986. Conversion of proinsulin to insulin occurs coordinately with acidification of maturing secretory vesicles. J Cell Biol 103:2273–2281.

5. Arvan P, Castle D. 1998. Sorting and storage during secretory granule biogenesis: looking backward and looking forward. Biochem J 332 (Pt 3):593–610.

6. Chanat E, Huttner WB. 1991. Milieu-induced, selective aggregation of regulated secretory proteins in the trans-Golgi network. J Cell Biol 115:1505–19.

7. Huizing M, Helip-Wooley A, Westbroek W, Gunay-Aygun M, Gahl WA. 2008. Disorders of lysosome-related organelle biogenesis: clinical and molecular genetics. Annu Rev Genomics Hum Genet 9:359–386.

8. Marks MS, Heijnen HFG, Raposo G. 2013. Lysosome-related organelles: unusual compartments become mainstream. Curr Opin Cell Biol 25:495–505.

9. Luzio JP, Hackmann Y, Dieckmann NMG, Griffiths GM. 2014. The biogenesis of lysosomes and lysosome-related organelles. Cold Spring Harb Perspect Biol 6.

10. Bonifacino JS. 2004. Insights into the biogenesis of lysosome-related organelles from the study of the Hermansky-Pudlak syndrome. Ann N Y Acad Sci 1038:103–114.

11. Briguglio JS, Kumar S, Turkewitz AP. 2013. Lysosomal sorting receptors are essential for secretory granule biogenesis in Tetrahymena. J Cell Biol 203:537–550.

12. Raposo G, Marks MS, Cutler DF. 2007. Lysosome-related organelles: driving post-Golgi compartments into specialisation. Curr Opin Cell Biol 19:394–401.

13. Delevoye C, Marks MS, Raposo G. 2019. Lysosome-related organelles as functional adaptations of the endolysosomal system. Curr Opin Cell Biol 59:147–158.

14. Khawar MB, Gao H, Li W. 2019. Mechanism of Acrosome Biogenesis in Mammals. Front Cell Dev Biol 7.

15. Le L, Sirés-Campos J, Raposo G, Delevoye C, Marks MS. 2021. Melanosome Biogenesis in the Pigmentation of Mammalian Skin. Integr Comp Biol 61:1517–1545.

16. McCormack JJ, Lopes da Silva M, Ferraro F, Patella F, Cutler DF. 2017. Weibel−Palade bodies at a glance. J Cell Sci 130:3611–3617.

17. Metcalf DJ, Nightingale TD, Zenner HL, Lui-Roberts WW, Cutler DF. 2008. Formation and function of Weibel-Palade bodies. J Cell Sci 121:19–27.

18. EC D, C M, S C, JS B. 2000. Lysosome-related organelles. FASEB J 14:1265–1278.

19. Gautam R, Novak EK, Tan J, Wakamatsu K, Ito S, Swank RT. 2006. Interaction of Hermansky-Pudlak Syndrome Genes in the Regulation of Lysosome-Related Organelles. Traffic 7:779–792.

20. Hermey G. 2009. The Vps10p-domain receptor family. Cell Mol Life Sci 66:2677–2689.

21. Kaur H, Sparvoli D, Osakada H, Iwamoto M, Haraguchi T, Turkewitz AP. 2017. An endosomal syntaxin and the AP-3 complex are required for formation and maturation of candidate lysosome-related secretory organelles (mucocysts) in Tetrahymena thermophila. Mol Biol Cell 28:1551–1564.

22. Starcevic M, Nazarian R, Dell'Angelica EC. 2002. The molecular machinery for the biogenesis of lysosome-related organelles: lessons from Hermansky-Pudlak syndrome. Semin Cell Dev Biol 13:271–278.

23. Wasmeier C, Romao M, Plowright L, Bennett DC, Raposo G, Seabra MC. 2006. Rab38 and Rab32 control post-Golgi trafficking of melanogenic enzymes. J Cell Biol 175:271–281.

24. Grabner CP, Price SD, Lysakowski A, Cahill AL, Fox AP. 2006. Regulation of large dense-core vesicle volume and neurotransmitter content mediated by adaptor protein 3. Proc Natl Acad Sci U S A 103:10035–10040.

25. Asensio CS, Sirkis DW, Edwards RH. 2010. RNAi screen identifies a role for adaptor protein AP-3 in sorting to the regulated secretory pathway. Journal of Cell Biology 191:1173–1187.

26. Ferraro F, Kriston-Vizi J, Metcalf DJ, Martin-Martin B, Freeman J, Burden JJ, Westmoreland D, Dyer CE, Knight AE, Ketteler R, Cutler DF. 2014. A Two-Tier Golgi-Based Control of Organelle Size Underpins the Functional Plasticity of Endothelial Cells. Dev Cell 29:292–304.

27. Hannah MJ, Williams R, Kaur J, Hewlett LJ, Cutler DF. 2002. Biogenesis of Weibel–Palade bodies. Semin Cell Dev Biol 13:313–324.

28. Hao Z, Wei L, Feng Y, Chen X, Du W, Ma J, Zhou Z, Chen L, Li W. 2015. Impaired maturation of large dense-core vesicles in muted-deficient adrenal chromaffin cells. J Cell Sci 128:1365–1374.

29. Sirkis DW, Edwards RH, Asensio CS. 2013. Widespread Dysregulation of Peptide Hormone Release in Mice Lacking Adaptor Protein AP-3. PLoS Genet 9:e1003812.

30. Bowman SL, Bi-Karchin J, Le L, Marks MS. 2019. The road to lysosome-related organelles: Insights from Hermansky-Pudlak syndrome and other rare diseases. Traffic 20:404–435.

31. Sparvoli D, Richardson E, Osakada H, Lan X, Iwamoto M, Bowman GR, Kontur C, Bourland WA, Lynn DH, Pritchard JK, Haraguchi T, Dacks JB, Turkewitz AP. 2018. Remodeling the Specificity of an Endosomal CORVET Tether Underlies Formation of Regulated Secretory Vesicles in the Ciliate Tetrahymena thermophila. Curr Biol 28:697-710.e13.

32. Kumar S, Briguglio JS, Turkewitz AP. 2014. An aspartyl cathepsin, CTH3, is essential for proprotein processing during secretory granule maturation in Tetrahymena thermophila. Mol Biol Cell 25:2444–2460.

33. Hermann GJ, Schroeder LK, Hieb CA, Kershner AM, Rabbitts BM, Fonarev P, Grant BD, Priess JR. 2005. Genetic analysis of lysosomal trafficking in Caenorhabditis elegans. Mol Biol Cell 16:3273–3288.

34. Kantheti P, Qiao X, Diaz ME, Peden AA, Meyer GE, Carskadon SL, Kapfhamer D, Sufalko D, Robinson MS, Noebels JL, Burmeister M. 1998. Mutation in AP-3 delta in the mocha mouse links endosomal transport to storage deficiency in platelets, melanosomes, and synaptic vesicles. Neuron 21:111–122.

35. Mullins C, Hartnell LM, Bonifacino JS. 2000. Distinct requirements for the AP-3 adaptor complex in pigment granule and synaptic vesicle biogenesis in Drosophila melanogaster. Mol Gen Genet 263:1003–1014.

36. Bowman GR, Elde NC, Morgan G, Winey M, Turkewitz AP. 2005. Core formation and the acquisition of fusion competence are linked during secretory granule maturation in Tetrahymena. Traffic 6:303–323.

37. Cowan AT, Bowman GR, Edwards KF, Emerson JJ, Turkewitz AP. 2005. Genetic, genomic, and functional analysis of the granule lattice proteins in Tetrahymena secretory granules. Mol Biol Cell 16:4046–4060.

38. BOWMAN GR, SMITH DGS, MICHAEL SIU KW, PEARLMAN RE, TURKEWITZ AP. 2005. Genomic and Proteomic Evidence for a Second Family of Dense Core Granule Cargo Proteins in *Tetrahymena thermophila*. Journal of Eukaryotic Microbiology 52:291–297.

39. Kumar S, Briguglio JS, Turkewitz AP. 2015. Secretion of Polypeptide Crystals from Tetrahymena thermophila Secretory Organelles (Mucocysts) Depends on Processing by a Cysteine Cathepsin, Cth4p. Eukaryot Cell 14:817–833.

40. Breton S, Brown D. 2013. Regulation of Luminal Acidification by the V-ATPase. Physiology 28:318–329.

41. Toei M, Saum R, Forgac M. 2010. Regulation and isoform function of the V-ATPases. Biochemistry 49:4715–23.

42. Luo Y, Scholl S, Doering A, Zhang Y, Irani NG, Di Rubbo S, Neumetzler L, Krishnamoorthy P, Van Houtte I, Mylle E, Bischoff V, Vernhettes S, Winne J, Friml J, Stierhof YD, Schumacher K, Persson S, Russinova E. 2015. V-ATPase activity in the TGN/EE is required for exocytosis and recycling in Arabidopsis. Nat Plants 1.

43. Stasic AJ, Chasen NM, Dykes EJ, Vella SA, Asady B, Starai VJ, Moreno SNJ. 2019. The Toxoplasma Vacuolar H+-ATPase Regulates Intracellular pH and Impacts the Maturation of Essential Secretory Proteins. Cell Rep 27:2132-2146.e7.

44. Wang Q, Wolf A, Ozkan S, Richert L, Mely Y, Chasserot-Golaz S, Ory S, Gasman S, Vitale N. 2023. V-ATPase modulates exocytosis in neuroendocrine cells through the activation of the ARNO-Arf6-PLD pathway and the synthesis of phosphatidic acid. Front Mol Biosci 10.

45. Hirao J, Tojo A, Hatakeyama S, Satonaka H, Ishimitsu T. 2020. V-ATPase blockade reduces renal gluconeogenesis and improves insulin secretion in type 2 diabetic rats. Hypertens Res 43:1079–1088.

46. Nakanishi-Matsui M, Matsumoto N, Sun-Wada GH, Wada Y. 2024. Role of the Cytosolic Domain of the a3 Subunit of V-ATPase in the Interaction with Rab7 and Secretory Lysosome Trafficking in Osteoclasts. Biol Pharm Bull 47:339–344.

47. Dai FF, Bhattacharjee A, Liu Y, Batchuluun B, Zhang M, Wang XS, Huang X, Luu L, Zhu D, Gaisano H, Wheeler MB. 2015. A Novel GLP1 Receptor Interacting Protein ATP6ap2 Regulates Insulin Secretion in Pancreatic Beta Cells. Journal of Biological Chemistry 290:25045–25061.

48. Fang Y, Feng H, Zhang B, Zhang S, Zhou Y, Hao P, Zhou Z, Zhou S, Li N, Hui Y, Ma L, Xiong J, Wu J, Liu L, Zhang X. 2024. Cytosolic pH is a direct nexus in linking environmental cues with insulin processing and secretion in pancreatic β cells. Cell Metab 36:1237-1251.e4.

49. Hutton JC. 1994. Insulin secretory granule biogenesis and the proinsulin-processing endopeptidases. Diabetologia 37 Suppl 2.

50. Futai M, Sun-Wada GH, Wada Y, Matsumoto N, Nakanishi-Matsui M. 2019. Vacuolar-type ATPase: A proton pump to lysosomal trafficking. Proc Jpn Acad Ser B Phys Biol Sci 95:261–277.

51. Parra KJ, Chan C-Y, Chen J. 2014. Saccharomyces cerevisiae vacuolar H+-ATPase regulation by disassembly and reassembly: one structure and multiple signals. Eukaryot Cell 13:706–14.

52. Oot RA, Couoh-Cardel S, Sharma S, Stam NJ, Wilkens S. 2017. Breaking up and making up: The secret life of the vacuolar H+ -ATPase. Protein Sci 26:896–909.

53. Chan C-Y, Parra KJ. 2014. Yeast phosphofructokinase-1 subunit Pfk2p is necessary for pH homeostasis and glucose-dependent vacuolar ATPase reassembly. J Biol Chem 289:19448–57.

54. Trombetta ES, Ebersold M, Garrett W, Pypaert M, Mellman I. 2003. Activation of lysosomal function during dendritic cell maturation. Science 299:1400–3.

55. Sautin YY, Lu M, Gaugler A, Zhang L, Gluck SL. 2005. Phosphatidylinositol 3-kinase-mediated effects of glucose on vacuolar H+-ATPase assembly, translocation, and acidification of intracellular compartments in renal epithelial cells. Mol Cell Biol 25:575–89.

56. Stransky LA, Forgac M. 2015. Amino Acid Availability Modulates Vacuolar H+-ATPase Assembly. J Biol Chem 290:27360–27369.

57. Bodzęta A, Kahms M, Klingauf J. 2017. The Presynaptic v-ATPase Reversibly Disassembles and Thereby Modulates Exocytosis but Is Not Part of the Fusion Machinery. Cell Rep 20:1348–1359.

58. Parra KJ, Kane PM. 1998. Reversible association between the V1 and V0 domains of yeast vacuolar H+-ATPase is an unconventional glucose-induced effect. Mol Cell Biol 18:7064–74.

59. Khan MM, Lee S, Couoh-Cardel S, Oot RA, Kim H, Wilkens S, Roh S-H. 2022. Oxidative stress protein Oxr1 promotes V-ATPase holoenzyme disassembly in catalytic activity-independent manner. EMBO J 41:e109360.

60. Lafourcade C, Sobo K, Kieffer-Jaquinod S, Garin J, van der Goot FG. 2008. Regulation of the V-ATPase along the endocytic pathway occurs through reversible subunit association and membrane localization. PLoS One 3:e2758.

61. Xu T, Forgac M. 2001. Microtubules are involved in glucose-dependent dissociation of the yeast vacuolar [H+]-ATPase in vivo. J Biol Chem 276:24855–61.

62. Lu M, Ammar D, Ives H, Albrecht F, Gluck SL. 2007. Physical interaction between aldolase and vacuolar H+-ATPase is essential for the assembly and activity of the proton pump. J Biol Chem 282:24495–503.

63. Smardon AM, Nasab ND, Tarsio M, Diakov TT, Kane PM. 2015. Molecular Interactions and Cellular Itinerary of the Yeast RAVE (Regulator of the H+-ATPase of Vacuolar and Endosomal Membranes) Complex. J Biol Chem 290:27511–23.

64. Lupanga U, Röhrich R, Askani J, Hilmer S, Kiefer C, Krebs M, Kanazawa T, Ueda T, Schumacher K. 2020. The Arabidopsis V-ATPase is localized to the TGN/EE via a seed plant-specific motif. Elife 9:1–40.

65. Chen Q, Kou H, Demy D Lou, Liu W, Li J, Wen Z, Herbomel P, Huang Z, Zhang W, Xu J. 2024. The different roles of V-ATPase a subunits in phagocytosis/endocytosis and autophagy. Autophagy https://doi.org/10.1080/15548627.2024.2366748.

66. Chu A, Zirngibl RA, Manolson MF. 2021. The V-ATPase a 3 Subunit: Structure, Function and Therapeutic Potential of an Essential Biomolecule in Osteoclastic Bone Resorption. Int J Mol Sci 22.

67. Forgac M. 2007. Vacuolar ATPases: rotary proton pumps in physiology and pathophysiology. Nat Rev Mol Cell Biol 8:917–929.

68. Sun-Wada G-H, Wada Y. 2013. Vacuolar-type proton pump ATPases: acidification and pathological relationships. Histol Histopathol 28:805–15.

69. Matsumoto N, Sekiya M, Tohyama K, Ishiyama-Matsuura E, Sun-Wada GH, Wada Y, Futai M, Nakanishi-Matsui M. 2018. Essential Role of the a3 Isoform of V-ATPase in Secretory Lysosome Trafficking via Rab7 Recruitment. Sci Rep 8.

70. Sun-Wada G-H, Wada Y. 2022. The a subunit isoforms of vacuolar-type proton ATPase exhibit differential distribution in mouse perigastrulation embryos. Sci Rep 12:13590.

71. Sun-Wada GH, Tabata H, Kawamura N, Futai M, Wada Y. 2007. Differential expression of a subunit isoforms of the vacuolar-type proton pump ATPase in mouse endocrine tissues. Cell Tissue Res 329:239–248.

72. Toyomura T, Murata Y, Yamamoto A, Oka T, Sun-Wada GH, Wada Y, Futai M. 2003. From lysosomes to the plasma membrane: localization of vacuolar-type H+ -ATPase with the a3 isoform during osteoclast differentiation. J Biol Chem 278:22023–22030.

73. Matsumoto N, Sekiya M, Sun-Wada G-H, Wada Y, Nakanishi-Matsui M. 2022. The lysosomal V-ATPase a3 subunit is involved in localization of Mon1-Ccz1, the GEF for Rab7, to secretory lysosomes in osteoclasts. Sci Rep 12:8455.

74. Kawasaki-Nishi S, Nishi T, Forgac M. 2001. Yeast V-ATPase complexes containing different isoforms of the 100-kDa a-subunit differ in coupling efficiency and in vivo dissociation. J Biol Chem 276:17941–17948.

75. Manolson MF, Wu B, Proteau D, Taillon BE, Roberts BT, Hoyt MA, Jones EW. 1994. STV1 gene encodes functional homologue of 95-kDa yeast vacuolar H(+)-ATPase subunit Vph1p. J Biol Chem 269:14064–14074.

76. Manolson MF, Proteau D, Preston RA, Stenbit A, Roberts BT, Hoyt MA, Preuss D, Mulholland J, Botstein D, Jones EW. 1992. The VPH1 gene encodes a 95-kDa integral membrane polypeptide required for in vivo assembly and activity of the yeast vacuolar H(+)-ATPase. Journal of Biological Chemistry 267:14294–14303.

77. Coyne RS, Thiagarajan M, Jones KM, Wortman JR, Tallon LJ, Haas BJ, Cassidy-Hanley DM, Wiley EA, Smith JJ, Collins K, Lee SR, Couvillion MT, Liu Y, Garg J, Pearlman RE, Hamilton EP, Orias E, Eisen JA, Methé BA. 2008. Refined annotation and assembly of the Tetrahymena thermophila genome sequence through EST analysis, comparative genomic hybridization, and targeted gap closure. BMC Genomics 9.

78. Eisen JA, Coyne RS, Wu M, Wu D, Thiagarajan M, Wortman JR, Badger JH, Ren Q, Amedeo P, Jones KM, Tallon LJ, Delcher AL, Salzberg SL, Silva JC, Haas BJ, Majoros WH, Farzad M, Carlton JM, Smith RK, Garg J, Pearlman RE, Karrer KM, Sun L, Manning

G, Elde NC, Turkewitz AP, Asai DJ, Wilkes DE, Wang Y, Cai H, Collins K, Stewart BA, Lee SR, Wilamowska K, Weinberg Z, Ruzzo WL, Wloga D, Gaertig J, Frankel J, Tsao CC, Gorovsky MA, Keeling PJ, Waller RF, Patron NJ, Cherry JM, Stover NA, Krieger CJ, Del Toro C, Ryder HF, Williamson SC, Barbeau RA, Hamilton EP, Orias E. 2006. Macronuclear genome sequence of the ciliate Tetrahymena thermophila, a model eukaryote. PLoS Biol 4:1620–1642.

79. Xiong J, Lu Y, Feng J, Yuan D, Tian M, Chang Y, Fu C, Wang G, Zeng H, Miao W. 2013. Tetrahymena functional genomics database (TetraFGD): an integrated resource for Tetrahymena functional genomics. Database (Oxford) 2013.

80. Miao W, Xiong J, Bowen J, Wang W, Liu Y, Braguinets O, Grigull J, Pearlman RE, Orias E, Gorovsky MA. 2009. Microarray Analyses of Gene Expression during the Tetrahymena thermophila Life Cycle. PLoS One 4:e4429.

81. Xiong J, Lu XY, Lu YM, Zeng HH, Yuan DX, Feng LF, Chang Y, Bowen J, Gorovsky M, Fu CJ, Miao W. 2011. Tetrahymena Gene Expression Database (TGED): a resource of microarray data and co-expression analyses for Tetrahymena. Sci China Life Sci 54:65–67.

82. Turkewitz AP, Bright LJ. 2011. A Rab-based view of membrane traffic in the ciliate *Tetrahymena thermophila*. Small GTPases 2:222–226.

83. Bright LJ, Kambesis N, Nelson SB, Jeong B, Turkewitz AP. 2010. Comprehensive Analysis Reveals Dynamic and Evolutionary Plasticity of Rab GTPases and Membrane Traffic in Tetrahymena thermophila. PLoS Genet 6:e1001155.

84. Satir B. 1977. Dibucaine-induced synchronous mucocyst secretion in Tetrahymena. Cell Biol Int Rep 1:69–73.

85. Turkewitz AP, Madeddu L, Kelly RB. 1991. Maturation of dense core granules in wild type and mutant Tetrahymena thermophila. EMBO J 10:1979–1987.

86. Lumpert CJ, Glas-Albrecht R, Eisenmann E, Plattner H. 1992. Secretory organelles of Paramecium cells (trichocysts) are not remarkably acidic compartments. J Histochem Cytochem 40:153–160.

87. Prakash P, Jethava KP, Korte N, Izquierdo P, Favuzzi E, Rose IVL, Guttenplan KA, Manchanda P, Dutta S, Rochet JC, Fishell G, Liddelow SA, Attwell D, Chopra G. 2021. Monitoring phagocytic uptake of amyloid β into glial cell lysosomes in real time. Chem Sci 12:10901–10918.

88. Benčina M. 2013. Illumination of the Spatial Order of Intracellular pH by Genetically Encoded pH-Sensitive Sensors. Sensors (Basel) 13:16736.

89. Martinière A, Desbrosses G, Sentenac H, Paris N. 2013. Development and properties of genetically encoded pH sensors in plants. Front Plant Sci 4.

90. Michaluk P, Rusakov DA. 2022. Monitoring cell membrane recycling dynamics of proteins using whole-cell fluorescence recovery after photobleaching of pH-sensitive genetic tags. Nat Protoc 17:3056–3079.

91. de Loubresse NG, Gautier M, Sperling L. 1994. Immature secretory granules are not acidic in *Paramecium* : Implications for sorting to the regulated pathway. Biol Cell 82:139–147.

92. Wassmer T, Kissmehl R, Cohen J, Plattner H. 2006. Seventeen a-subunit isoforms of paramecium V-ATPase provide high specialization in localization and function. Mol Biol Cell 17:917–30.

93. Wassmer T, Sehring IM, Kissmehl R, Plattner H. 2009. The V-ATPase in Paramecium: functional specialization by multiple gene isoforms. Pflugers Arch 457:599–607.

94. Wassmer T, Froissard M, Plattner H, Kissmehl R, Cohen J. 2005. The vacuolar proton-ATPase plays a major role in several membrane-bounded organelles in Paramecium. J Cell Sci 118:2813–25.

95. Oka T, Toyomura T, Honjo K, Wada Y, Futai M. 2001. Four subunit a isoforms of Caenorhabditis elegans vacuolar H+-ATPase. Cell-specific expression during development. J Biol Chem 276:33079–85.

96. Capecci J, Forgac M. 2013. The function of vacuolar ATPase (V-ATPase) a subunit isoforms in invasiveness of MCF10a and MCF10CA1a human breast cancer cells. J Biol Chem 288:32731–32741.

97. Poëa-Guyon S, Ammar MR, Erard M, Amar M, Moreau AW, Fossier P, Gleize V, Vitale N, Morel N. 2013. The V-ATPase membrane domain is a sensor of granular pH that controls the exocytotic machinery. J Cell Biol 203:283–298.

98. Paroutis P, Touret N, Grinstein S. 2004. The pH of the secretory pathway: measurement, determinants, and regulation. Physiology (Bethesda) 19:207–215.

99. Schoonderwoert VTG, Martens GJM. 2001. Proton pumping in the secretory pathway. J Membr Biol 182:159–169.

100. Cheng CY, Romero DP, Zoltner M, Yao MC, Turkewitz AP. 2023. Structure and dynamics of the contractile vacuole complex in Tetrahymena thermophila. J Cell Sci 136.

101. Stock C, Grønlien HK, Allen RD. 2002. The ionic composition of the contractile vacuole fluid of Paramecium mirrors ion transport across the plasma membrane. Eur J Cell Biol 81:505–515.

102. Heuser J, Zhu Q, Clarke M. 1993. Proton pumps populate the contractile vacuoles of Dictyostelium amoebae. J Cell Biol 121:1311–1327.

103. Correia MS, Moreiras H, Pereira FJC, Neto M V, Festas TC, Tarafder AK, Ramalho JS, Seabra MC, Barral DC. 2018. Melanin Transferred to Keratinocytes Resides in Nondegradative Endocytic Compartments. J Invest Dermatol 138:637–646.

104. Hurbain I, Romao M, Sextius P, Bourreau E, Marchal C, Bernerd F, Duval C, Raposo G. 2018. Melanosome Distribution in Keratinocytes in Different Skin Types: Melanosome Clusters Are Not Degradative Organelles. J Invest Dermatol 138:647–656.

105. Cheng X-T, Xie Y-X, Zhou B, Huang N, Farfel-Becker T, Sheng Z-H. 2018. Characterization of LAMP1-labeled nondegradative lysosomal and endocytic compartments in neurons. J Cell Biol 217:3127–3139.

106. Yap CC, Digilio L, McMahon LP, Garcia ADR, Winckler B. 2018. Degradation of dendritic cargos requires Rab7-dependent transport to somatic lysosomes. J Cell Biol 217:3141–3159.

107. Jimenez V, Docampo R. 2015. TcPho91 is a contractile vacuole phosphate sodium symporter that regulates phosphate and polyphosphate metabolism in Trypanosoma cruzi. Mol Microbiol 97:911–925.

108. Stock C, Allen RD, Naitoh Y. 2001. How external osmolarity affects the activity of the contractile vacuole complex, the cytosolic osmolarity and the water permeability of the plasma membrane in Paramecium multimicronucleatum. J Exp Biol 204:291–304.

109. Sava I, Davis LJ, Gray SR, Bright NA, Luzio JP. 2024. Reversible assembly and disassembly of V-ATPase during the lysosome regeneration cycle. Mol Biol Cell 35.

110. Graham LA, Hill KJ, Stevens TH. 1995. VMA8 encodes a 32-kDa V1 subunit of the Saccharomyces cerevisiae vacuolar H(+)-ATPase required for function and assembly of the enzyme complex. J Biol Chem 270:15037–44.

111. Xu T, Forgac M. 2000. Subunit D (Vma8p) of the Yeast Vacuolar H+-ATPase Plays a Role in Coupling of Proton Transport and ATP Hydrolysis. Journal of Biological Chemistry 275:22075–22081.

112. Jackson MB, Chapman ER. 2006. FUSION PORES AND FUSION MACHINES IN CA $^{2+}$ -TRIGGERED EXOCYTOSIS. Annu Rev Biophys Biomol Struct 35:135–160.

113. Merz AJ. 2015. What are the roles of V-ATPases in membrane fusion? Proc Natl Acad Sci U S A 112:8–9.

114. Sreelatha A, Bennett TL, Carpinone EM, O'Brien KM, Jordan KD, Burdette DL, Orth K, Starai VJ. 2015. Vibrio effector protein VopQ inhibits fusion of V-ATPase-containing membranes. Proc Natl Acad Sci U S A 112:100–105.

115. Nguyen JA, Yates RM. 2021. Better Together: Current Insights Into Phagosome-Lysosome Fusion. Front Immunol 12.

116. Hiesinger PR, Fayyazuddin A, Mehta SQ, Rosenmund T, Schulze KL, Zhai RG, Verstreken P, Cao Y, Zhou Y, Kunz J, Bellen HJ. 2005. The v-ATPase V0 subunit a1 is required for a late step in synaptic vesicle exocytosis in Drosophila. Cell 121:607–620.

117. Williamson WR, Wang D, Haberman AS, Hiesinger PR. 2010. A dual function of V0-ATPase a1 provides an endolysosomal degradation mechanism in Drosophila melanogaster photoreceptors. J Cell Biol 189:885–899.

118. Kuppannan A, Jiang YY, Maier W, Liu C, Lang CF, Cheng CY, Field MC, Zhao M, Zoltner M, Turkewitz AP. 2022. A novel membrane complex is required for docking and regulated exocytosis of lysosome-related organelles in Tetrahymena thermophila. PLoS Genet 18.

119. Rahaman A, Miao W, Turkewitz AP. 2009. Independent transport and sorting of functionally distinct protein families in Tetrahymena thermophila dense core secretory granules. Eukaryot Cell 8:1575–1583.

120. Bowman GR, Turkewitz AP. 2001. Analysis of a mutant exhibiting conditional sorting to dense core secretory granules in Tetrahymena thermophila. Genetics 159:1605–1616.

121. Turkewitz AP, Kelly RB. 1992. Immunocytochemical analysis of secretion mutants of Tetrahymena using a mucocyst-specific monoclonal antibody. Dev Genet 13:151–159.

122. Ota T. 2018. Grl1 Protein is a Candidate K Antigen in Tetrahymena thermophila. Protist 169:321–332.

123. Lizárraga F, Poincloux R, Romão M, Montagnac G, Le Dez G, Bonne I, Rigaill G, Raposo G, Chavrier P. 2009. Diaphanous-related formins are required for invadopodia formation and invasion of breast tumor cells. Cancer Res 69:2792–2800.

124. Kelley LA, Mezulis S, Yates CM, Wass MN, Sternberg MJE. 2015. The Phyre2 web portal for protein modeling, prediction and analysis. Nat Protoc 10:845–858.

Figure Legends

Figure 1. (A) Expression profiling identifies a subunit of the V-ATPase complex (V-ATPase-a1) that is highly coregulated with known mucocyst associated genes (*GRL1*, *GRT1* and *CTH3*). Transcript data were retrieved from the Tetrahymena Functional Genomics Database (TFGB). For plotting the profiles, each value was normalized to the respective gene's maximum expression level. (B) *In silico* predicted transmembrane domains (TMD) of V-ATPase-a1p. (C) Homology between the TMDs of V-ATPase-a1 and its paralogs a2-a6. The TMD5 of V-ATPase-a1p shows no significant homology with the corresponding TMDs in other paralogs. (D) Other paralogs of the *V-ATPase-a* subunit (*a2-a6*) are not coregulated with known mucocyst genes.

Figure 2. (A) Phylogenetic reconstruction of V-ATPase-a genes. The phylogenetic relationship between V-ATPases in ciliates [*T. thermophila* (TT), *Paramecium tetraurelia* (PT) and *Ichthyophthirius multifiliis* (IM)}, *Homo sapiens* (HS), *Danio rerio* (DR), *Caenorhabditis elegans* (CE), *Drosophila melanogaster* (DM), *Arabidopsis* spp. *(*A) and *Toxoplasma gondii* (TG)] deduced by maximum-likelihood. Accession numbers for all sequences are listed in Supplemental **Table S1**. (B) The predicted structure of V-ATPase-a1p of *Tetrahymena* by the web portal Phyre2. The image is colored by the rainbow from the N to the C terminus. (C-D) The predicted structure of V-ATPase-a1p of *Tetrahymena thermophila* (green), *Saccharomyces cerevisiae* (yellow) and *Mus musculus* (red) by AlphaFold structure prediction. V-ATPase-a1p structure of *Tetrahymena thermophila* superimposed with V-ATPase-a1p of *Saccharomyces cerevisiae* (C) and *Mus musculus* (D) by PyMOL software.

Figure 3. Expression and localization of V-ATPase-a1p. (A) In optical surface and cross section (left and right, respectively), cells expressing endogenously 2xmNeon-6c-myc-tagged V-ATPase-a1p subunit [V-ATPAse-a1p(N)] were acquired by confocal microscope using super resolution mode with low exposure condition. At the cell surface, linear arrays of fluorescent puncta correlate to docked mucocysts, which show up in cross sections of the same cells as elongated vesicles. The inset reveals that V-ATPase-a1p(N) accumulates in the docked mature mucocysts. (B) Cells expressing V-ATPase-a1p(N) were lysed in buffer containing detergent and immunoprecipitated using anti-c-Myc Agarose beads. Pull down samples were separated by SDS-PAGE and blotted with mouse monoclonal anti-c-myc antibody. Blots were incubated with anti-mouse-IgG-HRP for IP and developed by SuperSignal West Femto Maximum Sensitivity Substrate. The expected size-specific band was only found in the V-ATPase-a1p(N) lane. (C-D) Cells co-expressing endogenously V-ATPase-a1p(N) with either mucocyst marker Igr1p-3xmCherry (C) or Grl3p-3xmCherry (D). V-ATPase-a1p(N) and mucocyst markers Igr1p or Grl3p overlap extensively within docked mucocysts at the cell surface and cell cortex. Images are shown as single slices, for clarity. The inset, Ci, and Di depict co-localization of V-ATPase-a1p(N) with mucocyst markers. (E) Cartoon representing localization of V-ATPase-a1p(N) at cortical and non-cortical compartments of cells. (F) The mean

fluorescence intensity associated with cell (B1), cortical (B2), and non- cortical (B3) was measured and converted to integrated density. The majority of V-ATPase-a1p(N) fraction remains in the non-cortical compartments. (G) Non-cortical fraction of V-ATPase-a1p(N) shows some overlap with endosomal marker FM4-64. Cells expressing V-ATPase-a1p(N) were incubated for 5 min with 5μM FM4-64 and then washed with 10mM Tris media (pH 7.4). Images were acquired after 30-40 minutes after incubation. (H) Panel H shows some co-localization between V-ATPase-a1p(N) and FM4-64 within 40 minutes; the inset (H) is from panel G (top). (I) V-ATPase-a1p(N) and FM4-64 fluorescence intensity graphs along the length of the rectangle shown in panel G (top). The optical sections shown are cell surface and cross section. Scale bars, 10 μm.

Figure 4. V-ATPase-a1p(G) is not associated with Grl3p containing vesicles. (A) The cartoon illustrates the linearized construct and how the *VPS8a* gene is knocked out through homologous recombination. (B) Verification of *VPS8a* gene knockout by RT-PCR. Total RNA was isolated and processed for RT-PCR using primers listed in Supplemental **Table S2**. The absence of a band in the *VPS8a* lane indicates that the gene was completely removed. For control, *β-tubulin* was used. (C) In optical cell cross section, WT (top) and *Δvps8a* (bottom) cells co-expressing endogenously V-ATPase-a1p(G) with 3xmCherry-tagged Grl3p. (D) A sample of 10 non-overlapping images from panel C was used to calculate the percentage of overlap (Mander's coefficient) between Grl3p and V-ATPase-a1p(G) using the Fiji-JACoP plugin. The error bars show the SDs. (E) WT (top) and *Δvps8a* (bottom) cells expressing endogenously V-ATPase-a1p(G) were stained with anti-GFP and anti-Grt1 (4D11) antibodies. Inset shows co-localization between V-ATPase-a1p(G) and Grt1p. (F) The percentage of overlap (Mander's coefficient) between Grt1p and V-ATPase-a1p(G) was calculated as mentioned above. (G) In cell cross section, WT (top) and *Δvps8a* (bottom) cells expressing endogenously V-ATPase-a1p(G) were incubated FM4-64 as before. Images were acquired after 30-40 minutes after incubation. Inset reveals that V-ATPase-a1p(G) fraction is associated with endosomal marker FM4-64. (H) The percentage of overlap (Mander's coefficient) between V-ATPase-a1p(G) and endosomal marker FM4-64 was calculated as mentioned above. Scale bars, 10μm.

Figure 5. (A) The cartoon represents the linearized construct and how the *V-ATPase-a1* gene is knocked out by homologous recombination. The knockout construct is described in detail in the Material and Methods section. (B) Confirmation of *V-ATPase-a1* gene knockout by one step RT-PCR. Total RNA was extracted, processed for reverse transcription and amplified by PCR using primers listed in Supplemental **Table S2**. The absence of a band in the *Δv-atpase-a1* lane shows the gene was completely knocked out. *β-tubulin* was used as a control. (C) *V-ATPase-a1* is required for the mucocyst secretion. Cells are stimulated with secretagogue dibucaine to induce regulated exocytosis. Following centrifugation, a dense pellet of cells is formed, with an overlaying flocculent comprised of expanded dense cores of exocytosis mucocyst. The flocculent layer is delineated with a solid at the upper border and a dashed line at the lower border. Stimulated wildtype cells produce a flocculent layer (left), while *Δv-atpase-a1* cells are grossly deficient in mucocyst content and produce no apparent flocculent layer (right).

Figure 6. V-ATPase-a1p is essential for mucocyst biogenesis. (A) Docked mucocysts are visualized in fixed wild-type cells by mAb 5E9 that recognizes Grl3p (top panel i), and mAb 4D11 that recognizes Grt1p (lower panel iii). *Δv-atpase-a1* cells immunostained in parallel, shows less mucocyst signal (top ii and lower panel iv). Irregular shape of fluorescence puncta of Grl3p is mostly seen in cytoplasm, whereas less signal of Grt1p is found in cytoplasmic puncta in *Δv-atpase-a1*. Inset shows single docked mucocyst at cell

cortex. Scale bars, 10 μm. (B) Electron micrographs show mucocysts in both wild-type and *Δv-atpase-a1* cells. In wild-type cells, intermediate or immature mucocysts (labelled with blue asterisks) and docked mature mucocysts (labelled with red asterisks) were seen. In *Δv-atpase-a1* cells, only intermediate or immature mucocysts are observed. The inset displays a zoom view of mucocysts. Scale bars, 2 μm. (C-D) V-ATPase-a1p is required for processing of proGrl proteins. Cell lysates (5000 cell equivalents in C and 10,000 cell equivalents in D) were separated by SDS-PAGE and followed by Western blotting using antibodies against Grl1p and Grl3p, members of the GRL family. All Grl proteins are proteolytically processed in wild-type cells during the formation of the mucocyst dense core. (C) Western blotting using rabbit anti-Grl1p antibody. The mature processed Gr1p product is predominantly shown in wild-type cells, while the unprocessed precursor of Grl1p is seen in *Δv-atpase-a1* cells. (D) Same as C but western blotting with rabbit anti-Grl3p antibody. In both cases, the unprocessed (proGrl) and processed (Grl) forms of GRL proteins are shown.

Figure 7. The lumen of the mucocyst is not stably acidic in *Tetrahymena*. The optical sections shown are the cell cross and surface section. Confocal images are shown as single slices, for clarity. (A) Cells expressing mucocyst marker Igr1p-3xmCherry were incubated with Acridine orange (AO), as described in the material and method section. There is no considerable overlap between AO and Igr1p in immature mucocysts (non-cortical pools) and mature docked mucocysts at the cell surface and cell cortex. (B) Protonex Green, which labels acidic cell compartments, was incubated with cells expressing Grl3p-3xmCherry. No significant co-localization is seen between Protonex Green dye and mucocyst marker Grl3p. C) Cell lysates (60,000 cell equivalents) were separated using SDS-PAGE, transferred to PVDF and probed with anti-GFP mAb. Fusion proteins Grl3p-GFP and Grl3p-pHluorin bands recognized by the antibody are indicated by an asterisk. (D) Grl3p-GFP and Grl3p-pHluorin constructs were expressed at the native *GRL3* locus as gene replacements by the Neo4 drug resistance cassette. The Super ecliptic pHluorin (SEP) variant only emits fluorescence at pH 6.5 or higher. In cell surface and cross section (left and right, respectively), cells expressing either Grl3p-GFP or Grl3p-pHluorin are seen in docked mucocyst at the cell surface and cell cortex.

Figure 8. The V-ATPase complex in mature, but not immature, mucocysts lacks multiple subunits. (A) The co-localization of VMA subunits and Grl3p was measured using cell cross (left) and surface sections (right). For the former, the edge of the cross-sections was excluded (indicated by green boundary line in cartoon, left) in order to measure colocalization in non-cortical structures. The surface sections (right) were used to measure colocalization in cortical structures. To reduce false co-localization in cortical sections due to the bright signal from the contractile vacuole near the cell posterior, only the colocalization in the anterior ½ of the cell was measured. (B-D) Cells co-expressing 2xmNeon-tagged VMA1p (B), VMA8p (C), and VMA10p (D) with the mucocyst marker Grl3p-3xmCherry, all under their endogenous promoters. In both cross and surface sections, VMA subunits are localized at the contractile vacuoles (CVs) and in non-cortical puncta, as well as at the cell cortex. Co-localisation was measured using the Fiji-BIOP JACoP plugin, as shown in panel A. The color images at the bottom show co-localisation in selected non-cortical (cross section) and cortical compartments (surface section). Grey images showed co-localisation after adjusting the thresholds for the green and red channels. There was no co-localization of VMA subunits with Grl3p in mature, docked mucocysts at the cell cortex. In contrast, there was significant overlap between Grl3p and the VMA subunits in non-cortex compartments. (E-F). 20 non-overlapping images from panels B, C, D, and G were used to calculate the percentage of overlap (Mander's

coefficient) between Grl3p and V-ATPase subunits (VMA1p, VMA8p, VMA10p, and V-ATPase-a1p) in cortical (E) and non-cortical compartments (F). The error bars show the SDs. (G) Co-expression of V-ATPase-a1p endogenously tagged with 2xmNeon and Grl3p-3xmCherry. In the surface section, there was complete overlap between Grl3p and V-ATPase-a1p, in the docked mucocysts. There was also significant co-localization of V-ATPase-a1p and Grl3p in non-cortical structures, as seen in cross-sections of the same cells. Scale bars, 10 μm.

Figure 9. Mucocyst proteins Grl1p and Grt1p containing vesicles are not fused in *Δv-atpase-a1* cells. (A) Wild type Cu428 (top panel), *Δv-atpase-a1* (middle panel) and *Δvps8a* (bottom panel) cells were double stained with rabbit anti-Grl1 and mouse monoclonal anti-Grt1 (4D11). Co-localization of Grl1p and Grt1p is significantly reduced in *Δv-atpase-a1* and *Δvps8a* cells. *Δvps8a* cells used as positive control. The optical cross sections are shown as single slices, for clarity. Scale bars, 10 μm. (B) The Fiji-JACoP plugin was used to calculate the percentage of overlap (Mander's coefficient) between Grl1p and Grt1p using a sample of 26 non-overlapping images. The error bars show the SDs. (C) Wild-type (top panel) and *Δv-atpase-a1* (bottom panel) cells expressing Stx7l1p-GFP were double stained with rabbit anti-GFP and mouse monoclonal anti-Grt1(4D11) antibodies. In *Δv-atpase-a1* cells, there is a significant decrease in the co-localization of Stx7l1p and Grt1p. Inset shows co-localization between Stx7l1p and Grt1p. (D) A sample of ten non-overlapping pictures was used to determine the percentage of overlap (Mander's coefficient) between Stx7l1p and Grt1p using the Fiji-JACoP plugin, as mentioned above. (E) Wild-type (left panel) and *Δv-atpase-a1* (right panel) cells expressing Sor4p-GFP were double stained with rabbit anti-GFP and mouse monoclonal anti-Grt1 antibodies as before. (F) The Fiji-JACoP plugin was used to calculate the percentage of overlap (Mander's coefficient) between Sor4p and Grt1p as before. Scale bars, 10 μm. The noticeable difference in cell size between samples is due to variable flattening by the coverslips.

Figure 10. Proposed model for the mucocyst biogenesis pathway in *T. thermophila*, extending that proposed by Sparvoli et al., 2018. Both VPS8ap and Stx7l1p are required for homotypic and/or heterotypic fusion of pro-Grls and non-Grlp proteins containing vesicles to generate immature mucocysts, which then undergo maturation that depends on processing enzymes and the AP-3 adaptor. We now include V-ATPase-a1 in this model, and propose that it functions during mucocyst formation to promote homotypic and/or heterotypic fusion of Grl1p-containing and Grt1-containing vesicles. VMA subunits are lost from the V-ATPase complex during mucocyst maturation, and consequently the mature docked mucocysts are non-acidic.

Keywords
LRO, Mucocyst, V-ATPase-a1p, Holo-V-ATPase, Cth3p, pHluorin, VPS8ap, Rab7, DCG, Secretion, Exocytosis

Abbreviation
LRO: Lysosome-related organelle, DCG: Dense core granule, GFP: Green fluorescent protein, V-ATPase: Vacuolar-ATPase, SEP: Super-ecliptic pHluorin, Igr1: Induced during granule regeneration 1, VPS8: Vacuolar protein sorting 8, Stx7l1: Syntaxin 7-like 1, Grl: Granule lattice, Grt: Granule tip

Fig1

A

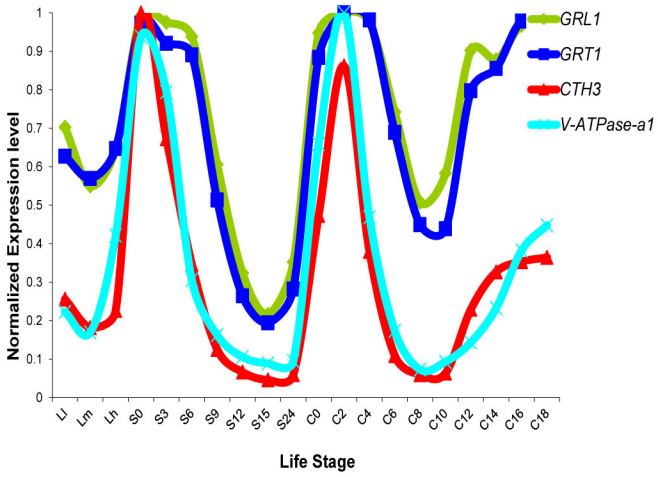

D

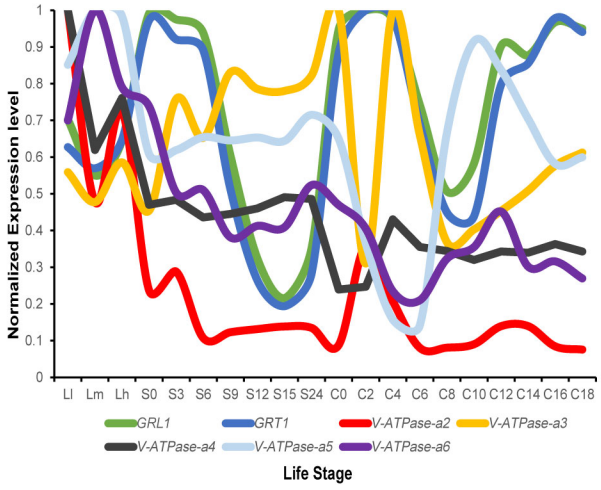

B

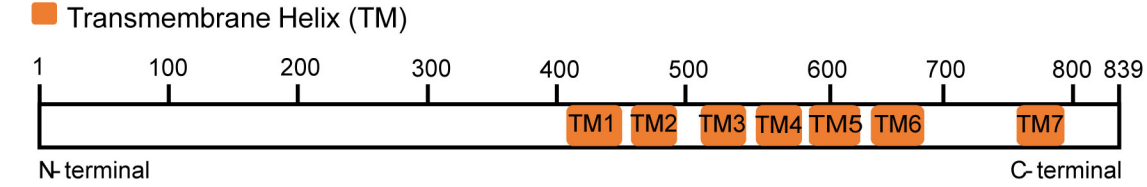

C

Transmembrane Helical (V-ATPase-a1p)	Sequence (V-ATPase-a1p)	TTHERM_01332070 V-ATPase-a1p	TTHERM_00463420 V-ATPase-a2p	TTHERM_00266570 V-ATPase-a3p	TTHERM_00372530 V-ATPase-a4p	TTHERM_01005210 V-ATPase-a5p	TTHERM_01014710 V-ATPase-a6p
TM1 414-440 amino acids	FFSIITFPFLFGVMFGDIGHGILLFTY	100%	80%	87.50%	87.50%	70%	63.60%
TM2 461-479 amino acids	CRYIISMMGFFAIFCGFIY	100%	55.60%	83.30%	83.30%	55.60%	50%
TM3 535-553 amino acids	SAIILGVSQMLLGILLKGL	100%	64.70%	No Homology	No Homology	66.70%	64.70%
TM4 565-587 amino acids	FFEFLPQLLFFICTFGYMALLII	100%	68.20%	No Homology	73.90%	59.10%	60.90%
TM5 599-616 amino acids	**APSILTIMLNFILNFGKL**	100%	44%	No Homology	No Homology	No Homology	No Homology
TM6 637-654 amino acids	LQFYLLIVAAVCVPLMLF	100%	64.30%	61.50%	71.40%	58.50%	68.80%
TM7 769-789 amino acids	SILGLLVGYFIFALITFGVLM	100%	61.90%	58.80%	65%	No Homology	No Homology

Fig2

A

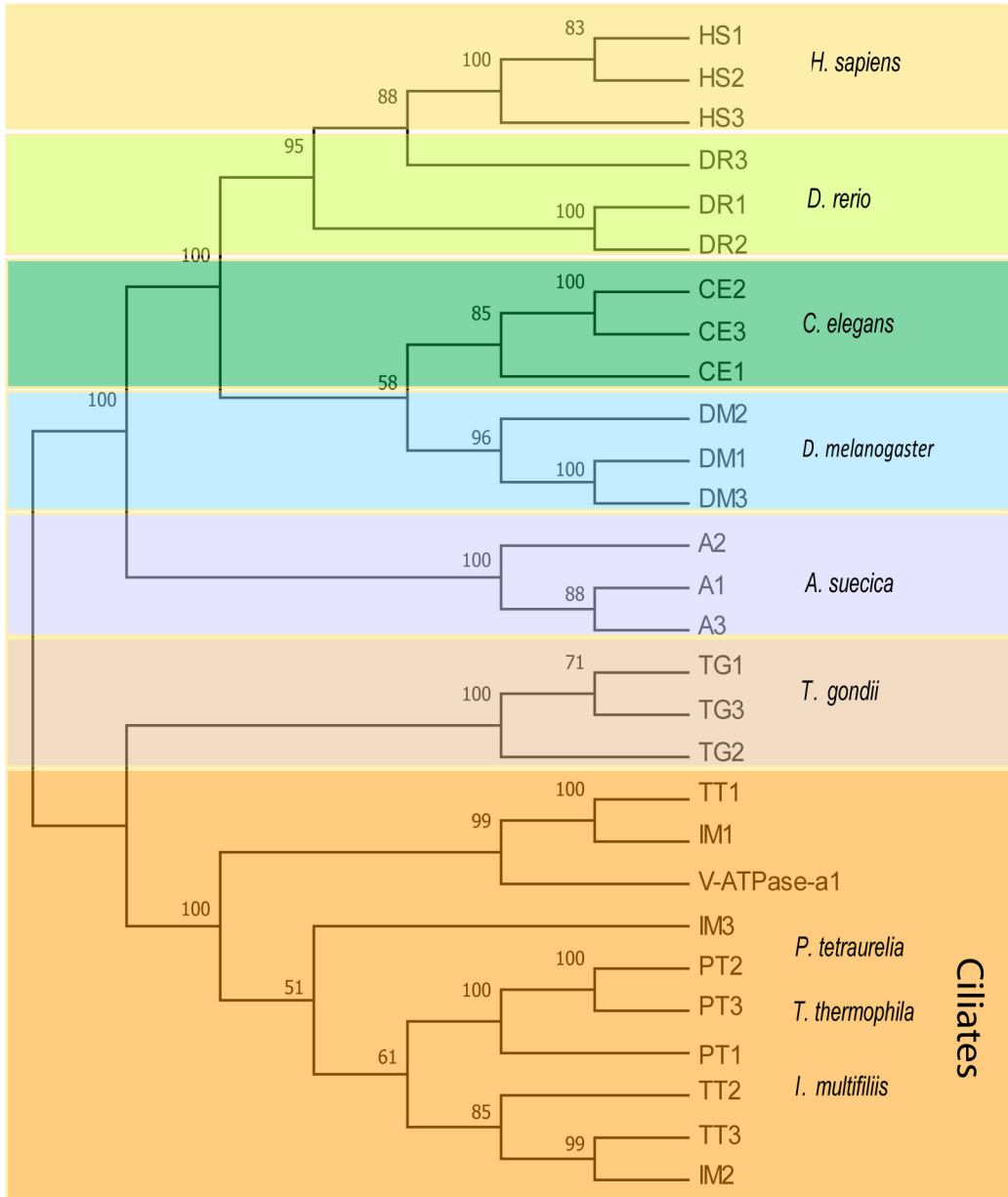
HS1
HS2
HS3
H. sapiens
DR3
DR1
DR2
D. rerio
CE2
CE3
CE1
C. elegans
DM2
DM1
DM3
D. melanogaster
A2
A1
A3
A. suecica
TG1
TG3
TG2
T. gondii
TT1
IM1
V-ATPase-a1
IM3
PT2
PT3
PT1
TT2
TT3
IM2
P. tetraurelia
T. thermophila
I. multifiliis
Ciliates
83
100
88
95
100
100
100
85
58
100
96
100
100
88
71
100
100
99
100
51
100
61
85
99

B

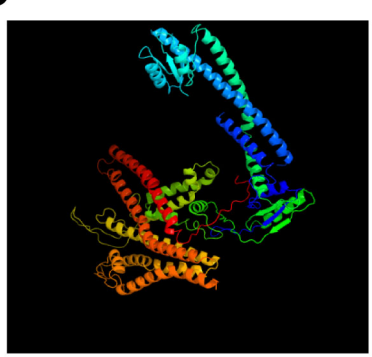

C

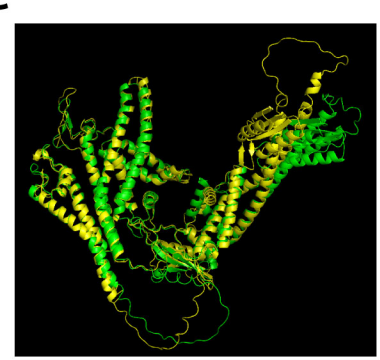

D

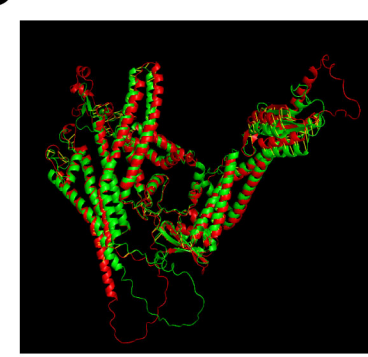

Fig3

A

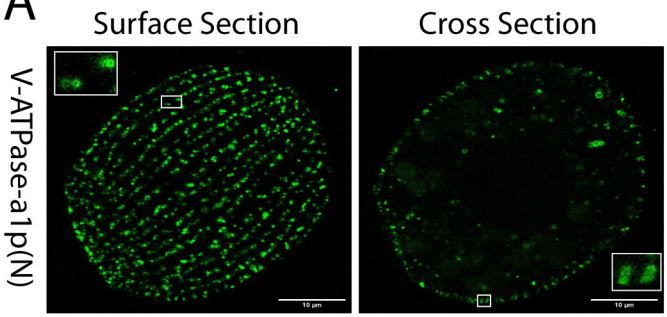

B

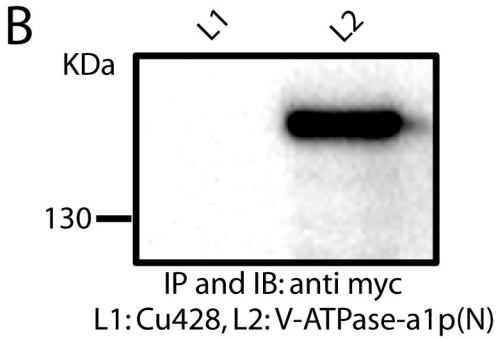

C

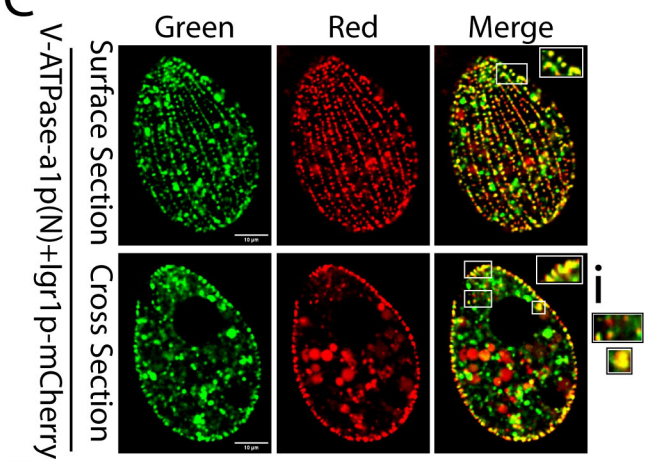

D

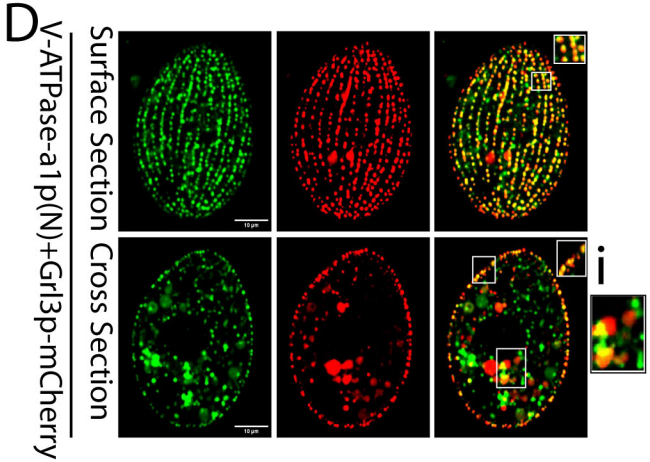

E

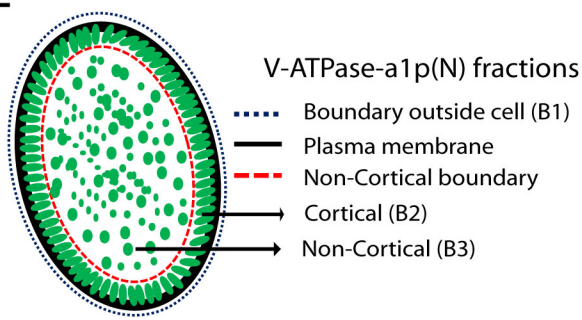

F

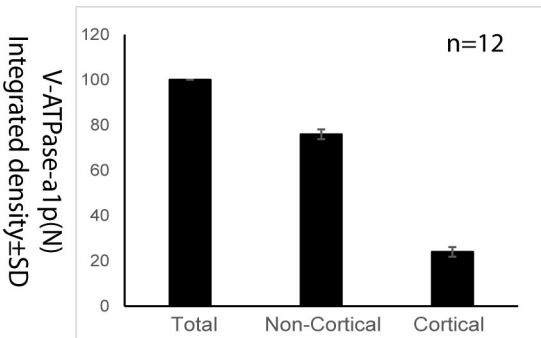

G

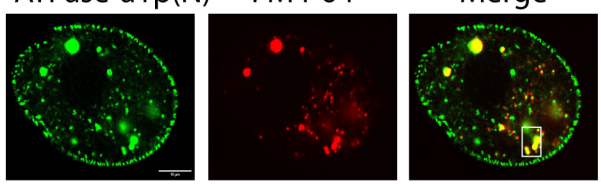

H

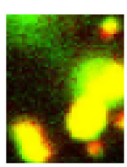

I

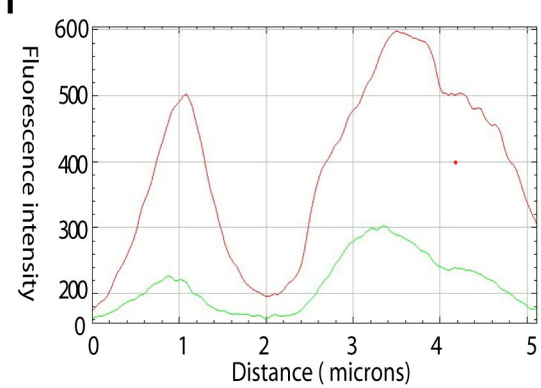

Fig4

A

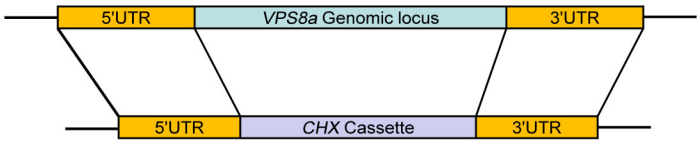

B

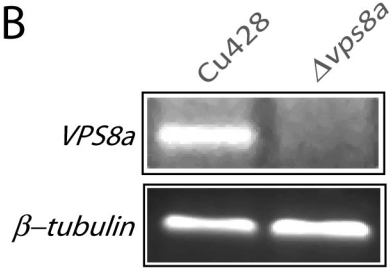

C

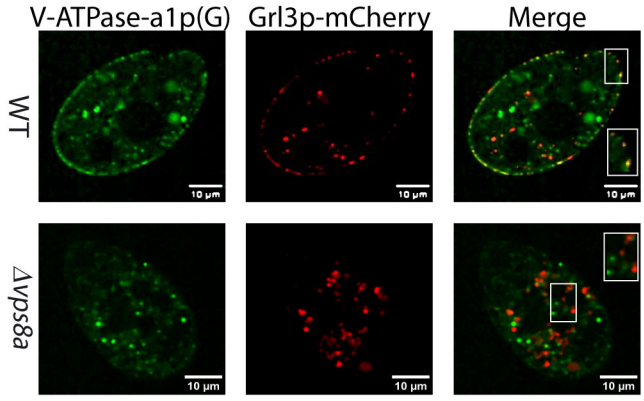

D

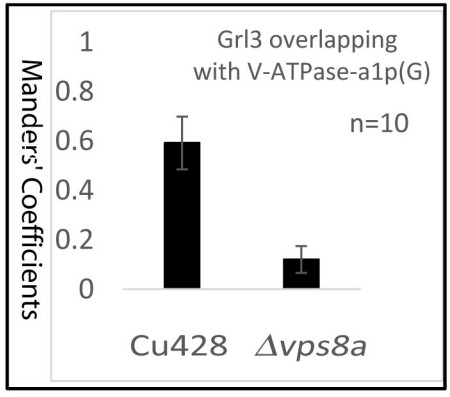

E

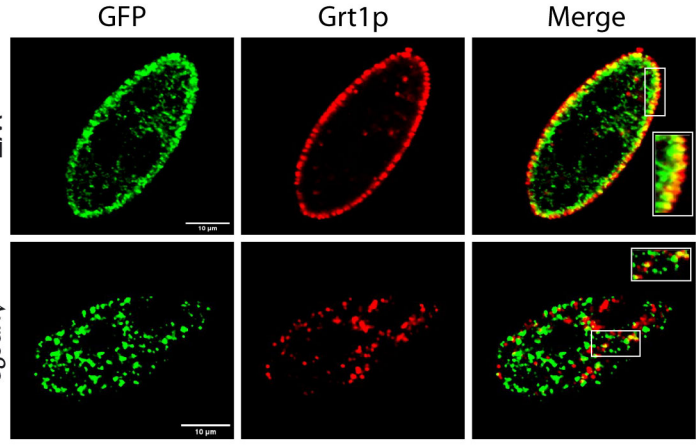

F

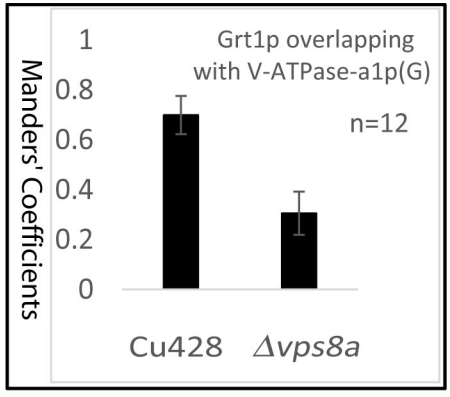

G

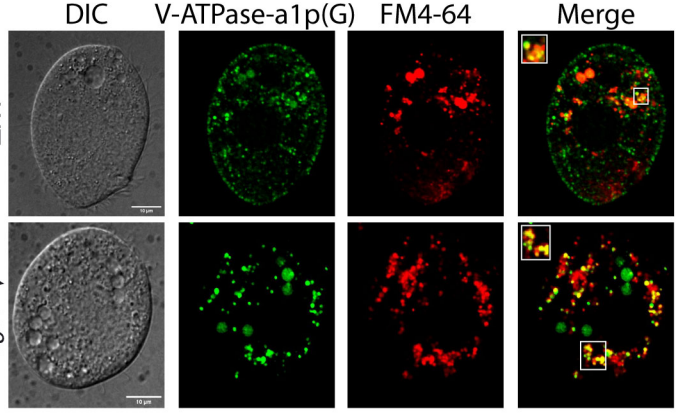

H

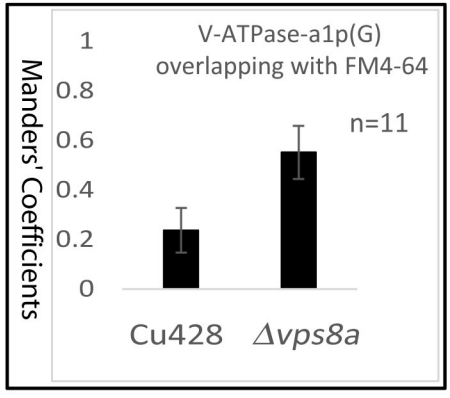

Fig5

A

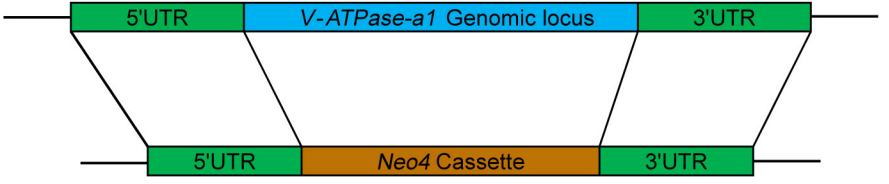
5'UTR
V-ATPase-a1 Genomic locus
3'UTR
5'UTR
Neo4 Cassette
3'UTR

B

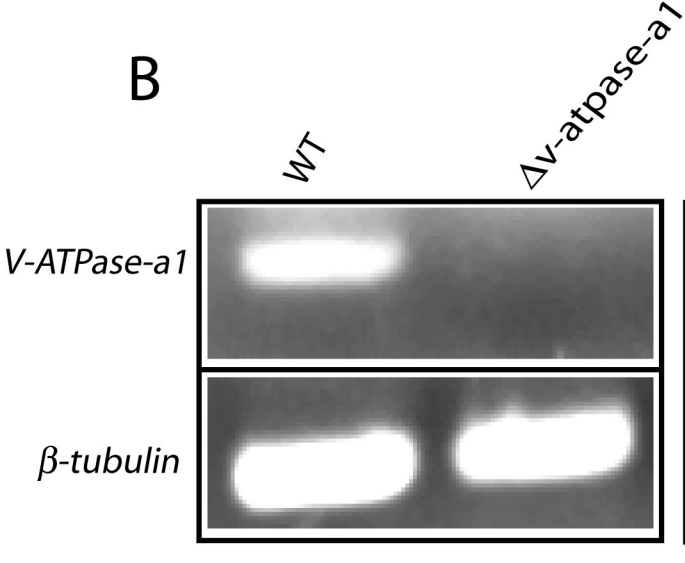
WT
Δv-atpase-a1
V-ATPase-a1
β-tubulin

C

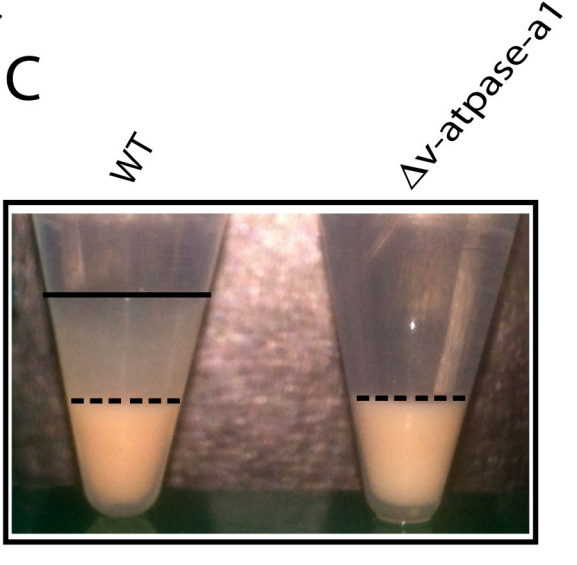
WT
Δv-atpase-a1

Fig6

A

DIC | Surface section | Cross section

Grl3p

i WT

ii Δv-atpase-a1

Grt1p

iii WT

iv Δv-atpase-a1

C

WT | Δv-atpase-a1

pro-Grl1p

Grl1p

IB: Rabbit Anti-Grl1 Antibody

D

WT | Δv-atpase-a1

pro-Grl3p

Grl3p

IB: Rabbit Anti-Grl3 Antibody

B

WT

i

ii

Δv-atpase-a1

iii

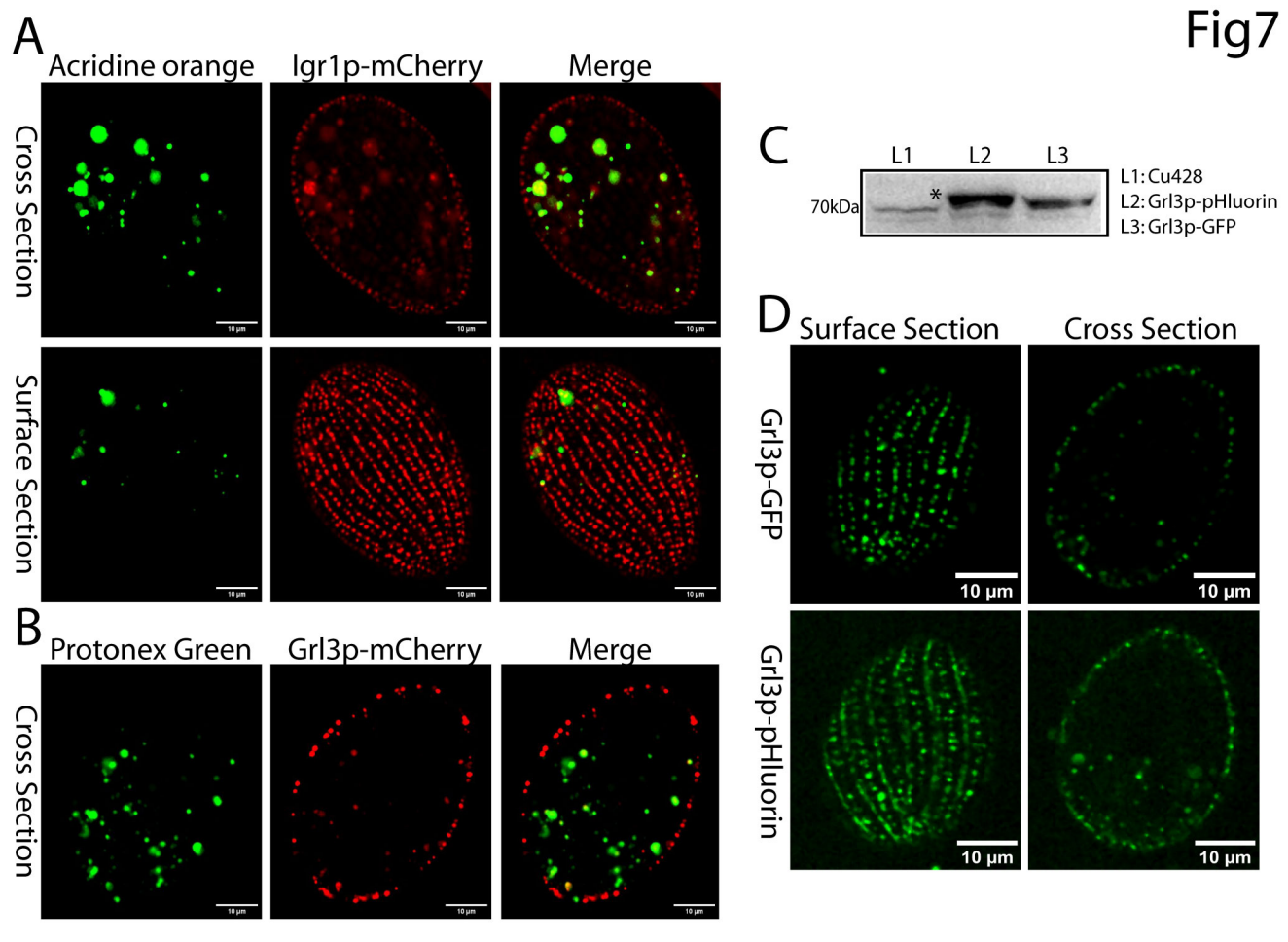
Fig7
A
Acridine orange
Igr1p-mCherry
Merge
Cross Section
Surface Section
B
Protonex Green
Grl3p-mCherry
Merge
Cross Section
C
L1
L2
L3
70kDa
*
L1: Cu428
L2: Grl3p-pHluorin
L3: Grl3p-GFP
D
Surface Section
Cross Section
Grl3p-GFP
Grl3p-pHluorin
10 µm

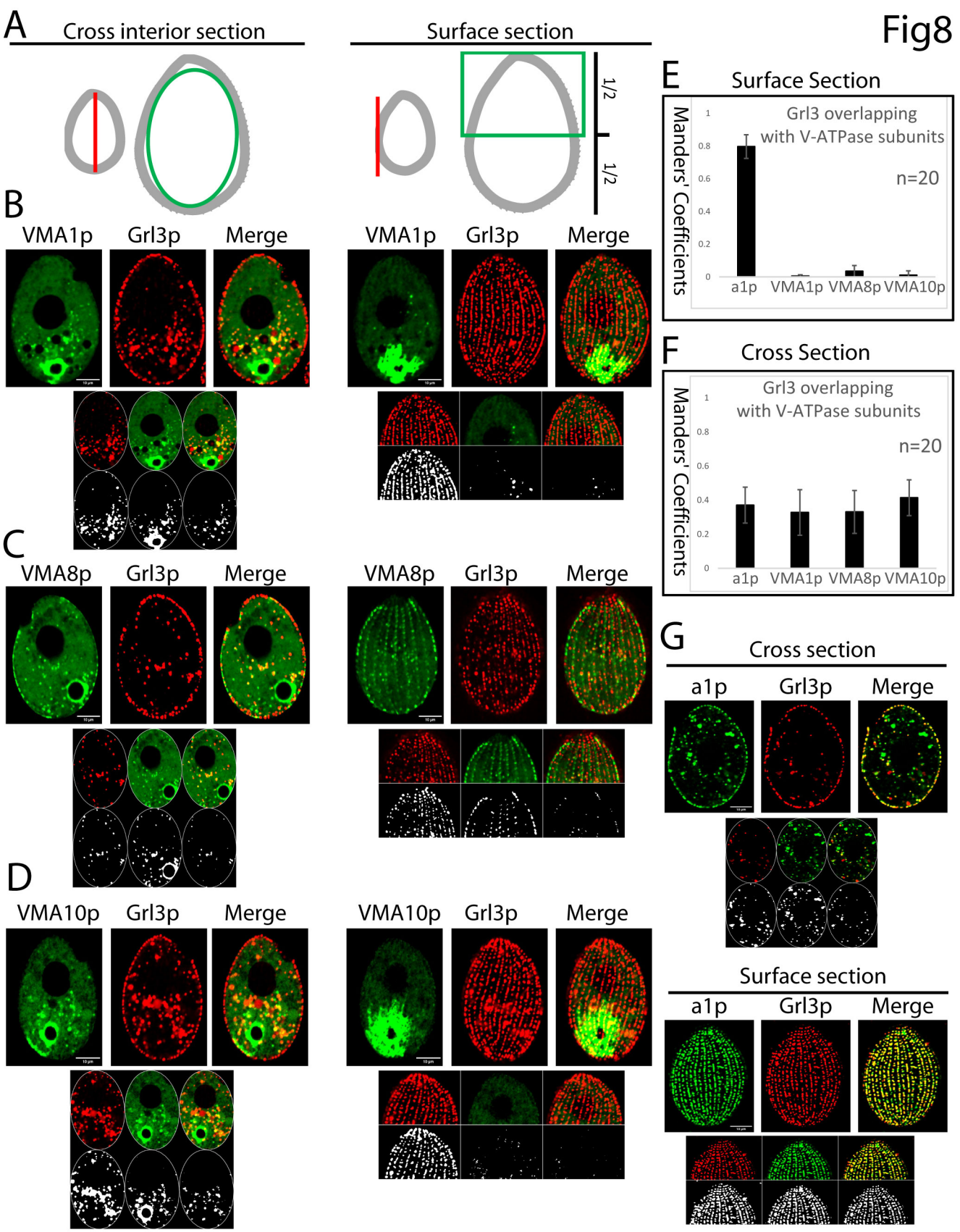
Fig8
A
Cross interior section
Surface section
1/2
1/2
B
VMA1p
Grl3p
Merge
VMA1p
Grl3p
Merge
C
VMA8p
Grl3p
Merge
VMA8p
Grl3p
Merge
D
VMA10p
Grl3p
Merge
VMA10p
Grl3p
Merge
E
Surface Section
Manders' Coefficients
Grl3 overlapping
with V-ATPase subunits
n=20
1
0.8
0.6
0.4
0.2
0
a1p
VMA1p
VMA8p
VMA10p
F
Cross Section
Manders' Coefficients
Grl3 overlapping
with V-ATPase subunits
n=20
1
0.8
0.6
0.4
0.2
0
a1p
VMA1p
VMA8p
VMA10p
G
Cross section
a1p
Grl3p
Merge
Surface section
a1p
Grl3p
Merge

Fig9

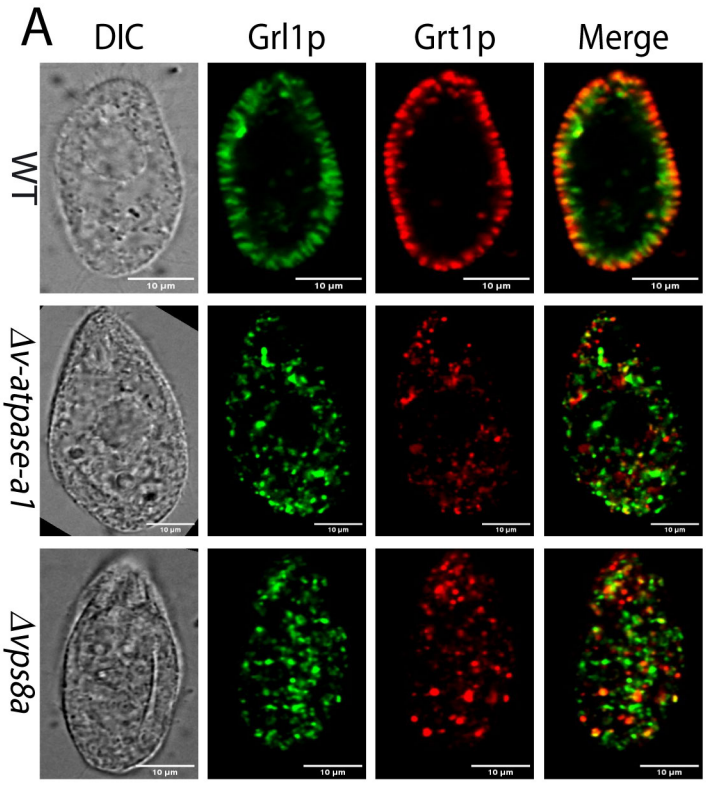
A
DIC
Grl1p
Grt1p
Merge
WT
Δv-atpase-a1
Δvps8a
10 µm

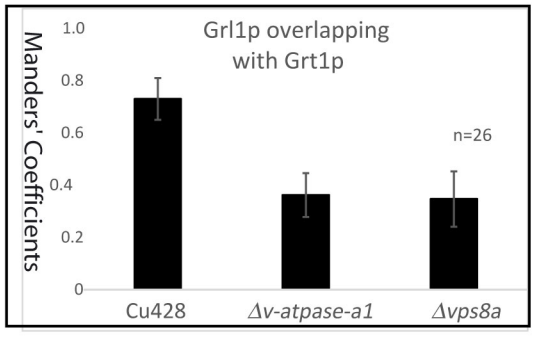
B
Grl1p overlapping with Grt1p
Manders' Coefficients
1.0
0.8
0.6
0.4
0.2
0
n=26
Cu428
Δv-atpase-a1
Δvps8a

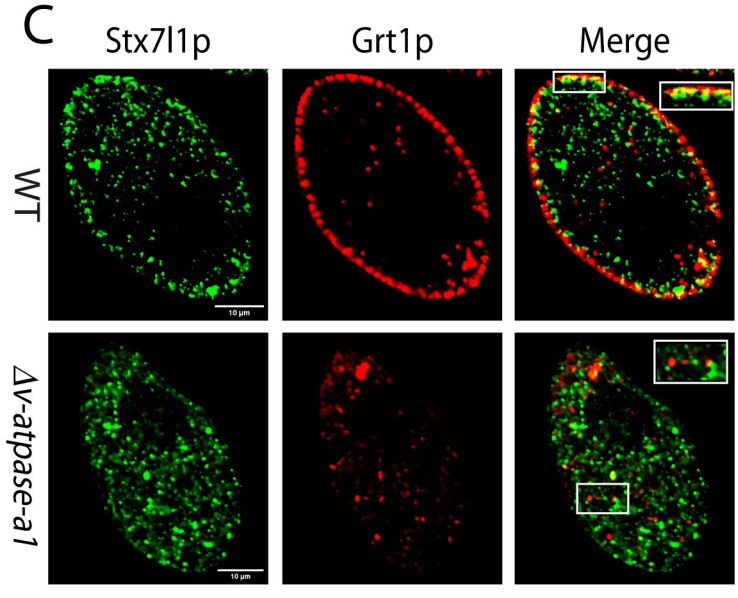
C
Stx7l1p
Grt1p
Merge
WT
Δv-atpase-a1
10 µm

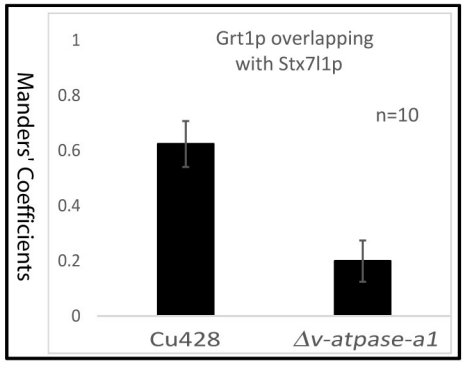
D
Grt1p overlapping with Stx7l1p
Manders' Coefficients
1
0.8
0.6
0.4
0.2
0
n=10
Cu428
Δv-atpase-a1

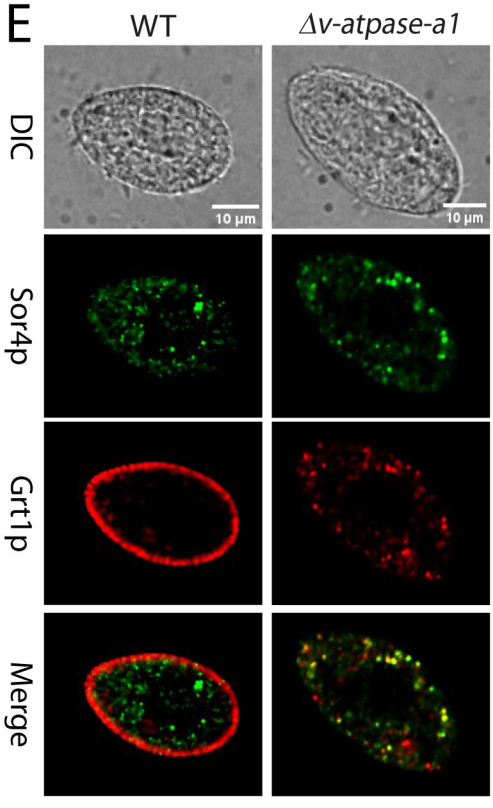
E
WT
Δv-atpase-a1
DIC
Sor4p
Grt1p
Merge
10 µm

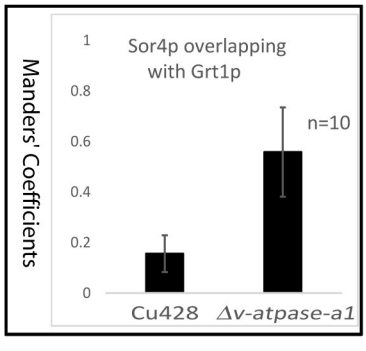
F
Sor4p overlapping with Grt1p
Manders' Coefficients
1
0.8
0.6
0.4
0.2
0
n=10
Cu428
Δv-atpase-a1

Fig10

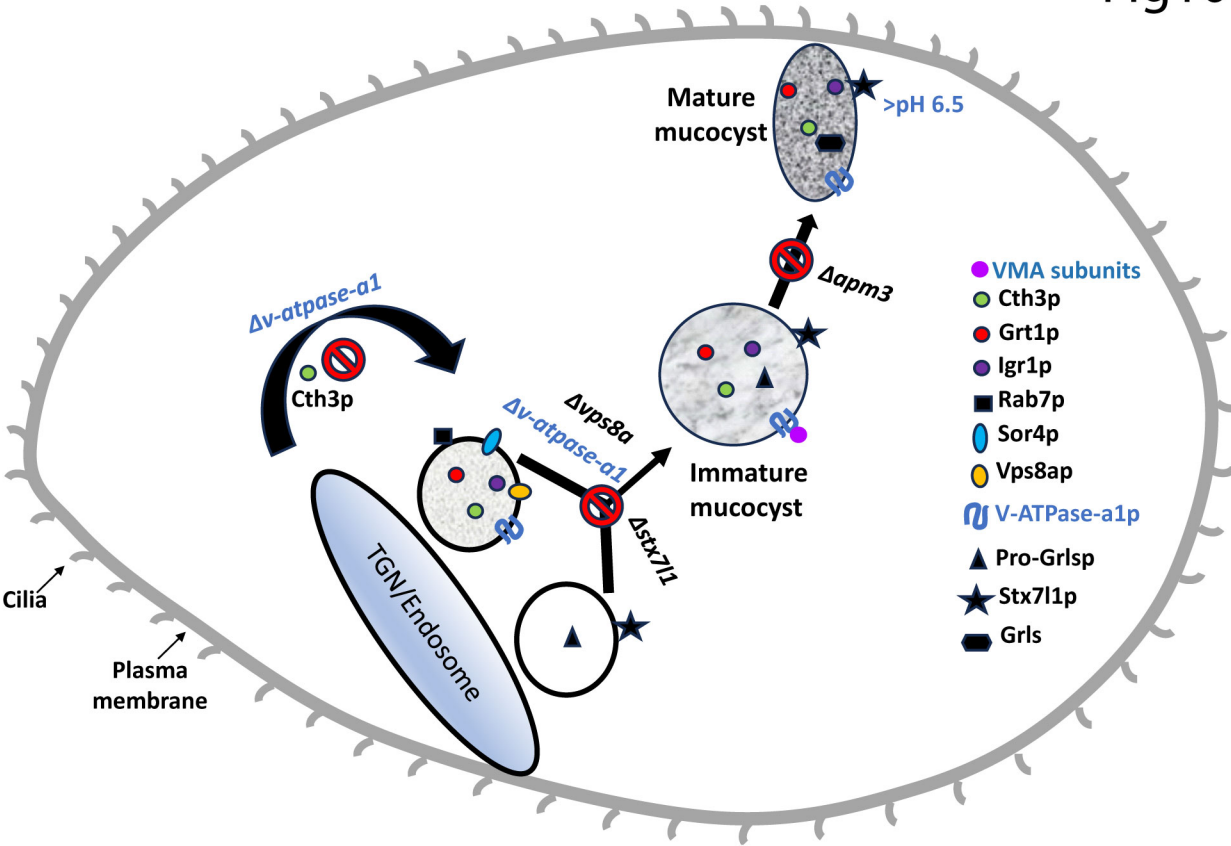
Mature mucocyst
>pH 6.5
Δapm3
Δv-atpase-a1
Cth3p
Δvps8a
Δv-atpase-a1
Immature mucocyst
Δstx7l1
TGN/Endosome
Cilia
Plasma membrane
VMA subunits
Cth3p
Grt1p
Igr1p
Rab7p
Sor4p
Vps8ap
V-ATPase-a1p
Pro-Grlsp
Stx7l1p
Grls